On the Importance of Model Selection for CFD Analysis of High Temperature Gas-Solid Reactive Flow; Case Study

Post Combustion Chamber of HIsarna Off-Gas System

Hosseini, A.; Hage, Johannes; Meijer, Koen; Offerman, S.E.; Yang, Y.

DOI
10.3390/pr11030839

Publication date
2023

Document Version
Final published version

Published in
Processes

Citation (APA)
Hosseini, A., Hage, J., Meijer, K., Offerman, S. E., & Yang, Y. (2023). On the Importance of Model Selection for CFD Analysis of High Temperature Gas-Solid Reactive Flow; Case Study: Post Combustion Chamber of HIsarna Off-Gas System . *Processes*, *11*(3), Article 839. https://doi.org/10.3390/pr11030839

processes

MDPI

Article

On the Importance of Model Selection for CFD Analysis of High Temperature Gas-Solid Reactive Flow; Case Study: Post Combustion Chamber of HIsarna Off-Gas System

Ashkan Hosseini [1,*], Johannes L. T. Hage [2], Koen Meijer [2], Erik Offerman [1] and Yongxiang Yang [1]

[1] Department of Materials Science and Engineering, Delft University of Technology, 2628 CN Delft, The Netherlands
[2] R&D Ironmaking, Tata Steel IJmuiden, 1951 JZ Velsen-Noord, The Netherlands
* Correspondence: a.hosseini-1@tudelft.nl

Abstract: In this paper a CFD analysis of HIsarna off-gas system for post combustion of CO-H2-carbon particle mixture is presented to evaluate the effect of different sub-models and parameters on the accuracy of predictions and simulation time. The effects of different mesh type, mesh grid size, radiation models, turbulent models, kinetic mechanism, turbulence chemistry interaction models, including and excluding gas-solid reactions, number of reactive solid particles are investigated in detail. Based on the accuracy of the predictions and agreement with counterpart measured values, the best combination is selected and conclusions are derived. It was found that radiation and turbulence chemistry interaction model have a major effect on the temperature and composition profile prediction along the studied off-gas system, compared to the variations in other models. The effect of these two models becomes even more evident when the temperature and fuel content of the flue gas are high.

Keywords: HIsarna ironmaking; CFD modelling; radiation modelling; combustion modelling; turbulence modelling; gas-solid reaction; turbulence-chemistry interaction

Citation: Hosseini, A.; Hage, J.L.T.; Meijer, K.; Offerman, E.; Yang, Y. On the Importance of Model Selection for CFD Analysis of High Temperature Gas-Solid Reactive Flow; Case Study: Post Combustion Chamber of HIsarna Off-Gas System. *Processes* **2023**, *11*, 839. https://doi.org/10.3390/pr11030839

Academic Editor: Udo Fritsching

Received: 1 February 2023
Revised: 23 February 2023
Accepted: 24 February 2023
Published: 10 March 2023

1. Introduction

CFD modelling is an iterative design process with large number of parametric variations [1–3]. Using CFD tools, it is possible to study almost any phenomena at any scale and complexity where knowledge of a spatial distribution of flow quantities is desired [4]. After setting up an initial CFD model, based on the post-processed results and comparison with available measured data (if there is any), one can decide to improve the model by including sub-models, tweaking boundary conditions, increasing mesh resolution and computational cell numbers etc. However, there is a trade-off between the complexity of a CFD model, prediction accuracy, and computational cost (simulation time). Figure 1 shows a graphical representation of the mentioned trade-off. The higher is the complexity, the higher will be the computational cost but, a greater accuracy and more detailed results can be obtained. There has been developments in CFD modelling approaches to optimize the solving procedure to acquire high details and accuracy with lower computational cost. One great example could be development of polyhedral cells or new iterative method which can noticeably reduce the simulation time while preserving the accuracy.

High temperature reactive flow is among the most complex and challenging processes in the industry to model. The most important factor in modeling reactive flow systems is to correctly predict the gaseous (volumetric) and gas–solid mixture reaction rate. It is required to model the volumetric and gas–solid reactions in such a way that the temperature and composition evolution along the system is predicted correctly. Proper sub-models such as convective and conductive heat transfer, turbulence, radiation etc., need to be included. However, reactions and mass transfer phenomena modelling is indispensable and plays a vital role to achieve a well-tuned CFD model that can properly predict the behavior of a reactive flow. In this study, pilot scale off-gas system of HIsarna ironmaking process is chosen as a case study to discuss the importance of CFD model complexity and sub-model selection on model predictions, accuracy, stability, and computational costs. A post combustion chamber is incorporated in the off-gas system to remove CO-H_2-carbon mixture in the flue gas coming from the main reactor.

The analysis begins with the effect of computational grid and cell type. Grid cell type, size, and orientation can significantly influence the simulation time, as well as the accuracy of the results and solution stability. There have been numerous studies on the effect of cell type on total mesh cell counts, mesh quality, simulation time, accuracy of prediction and residuals [5–10]. The most efficient and classic grid is called structured grid which is mostly composed of well-aligned hexahedral cells [11]. However, when it comes to complex geometries with sharp edges and curved boundaries, using structured type of grids reduces the mesh quality (low orthogonal quality and high skewness). Furthermore, structured grid generation is a time-consuming task which requires high engineering skills [11,12]. An alternative to structured grid is unstructured one in which tetrahedral cells are commonly used. This types of cells can be positioned and assembled freely within the computational domain. The main drawback of tetrahedral cells is their limitation to excessive stretch which in turn can significantly increase numbers of elements compared to structured grids [10]. One solution to reduce the cell count would be combining tetrahedral and polyhedral cells. This conversion results in considerable reduction in the cell count with an increase in grid quality and calculation accuracy [13].

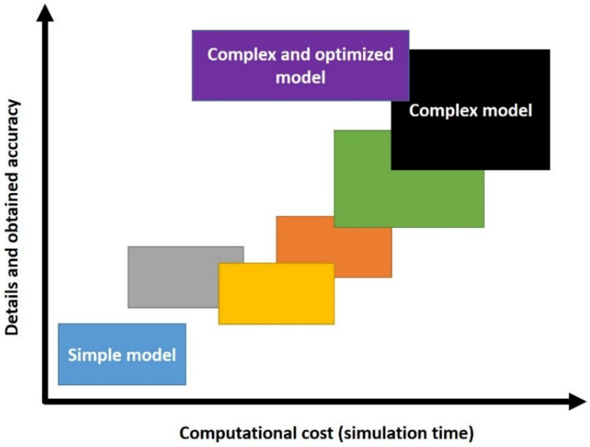

Figure 1. Trade-off between the complexity of the method and information content of results.

Selection of reaction mechanism is another important factor that can significantly affect the model predictions and costs. Reaction mechanism can have limited number of species and reactions involved which are usually referred to as global or multi step mechanisms. As an example, for mixture of CH_4-CO, Westbrook and Dryer [14,15] have proposed a simple three-step global mechanism that has been used in different research [16–20]. Novosselov and Malte [21] proposed another three-step mechanism in which the kinetic parameters are the function of pressure and temperature. Jones and Lindstedt [22] have proposed a four-step mechanism (JL mechanism), similar to WD mechanism, to include the effect of hydrogen content. On the contrary to the global mechanism, detailed mechanism is a set of elementary reactions forming a complex network. The most comprehensive detailed mechanism for combustion of CH_4-CO-H_2 mixture is known as GRI 3.0 (Gas Research Institute) originally designed by researchers at combustion laboratory of University of California, Berkeley [23]. The mechanism contains 55 species and 325 reaction which have been incorporated in CFD models to study CO-H_2 mixture (without CH_4 content) [24,25] and NOx formation [26–31]. To enhance the simulation speed, most of the researchers have used reduced GRI mechanisms where some species and therefore reactions are eliminated depending on the specific reactive flow conditions [32–36]. One reduced form of GRI mechanism is known as GRI 1.2 which contains 30 species and 177 reaction which will be used for comparison in this study. Other researcher have proposed their own detailed mechanism for CH_4-CO-H_2 mixture with much lower number of species and reactions; however, for kinetic data, they have mostly referred to the GRI mechanism [17,37–48]. There have been numerous studies on reaction mechanisms and development of kinetic database of CO-H_2 mixture combustion which are listed in Table A1 in the Appendix A.

Using detailed mechanism, it is possible to study different phenomena such as ignition temperature, ignition delay, laminar flame speed etc., which is not possible using global mechanisms.

Detailed mechanisms generally lead to a more reliable prediction in comparison to global mechanisms. Graca et al. [49] have studied the combustion of methane–air mixture using detailed mechanism and compared it to WD global mechanism and reported a poor performance and prediction of global mechanism. The same is reported by other researchers [43–45,50]. Frassoldati et al. [50] have performed a comparison of WD and JL global mechanisms with detailed mechanism in a laminar reactive flow. They have reported a large discrepancy between global mechanism and experimental temperature and composition profiles for a small-scale gas burner. Ultimately they have proposed a modified-JL mechanism by adding extra reactions with tuned kinetic parameters which matches well with predictions from both experiments and detailed mechanism. Nevertheless, the precisions of the detailed mechanism come at a higher computational cost as more species and reactions are include in the CFD calculations.

After selecting the reaction mechanism, a turbulence chemistry interaction model (TCI) also known as combustion model needs to be selected. A proper selection of TCI models has a substantial influence on the gas phase behavior and local/global composition and temperature distribution [51]. In this study, only eddy dissipation-based models are considered for selection and comparison. These models are eddy dissipation (EDM), finite rate eddy dissipation (FR-EDM), and eddy dissipation concept (EDC). There are extensive number of studies where TCI models have been utilized to simulate different gaseous and gas–solid reactive flow in both small and large-scale applications (listed in Table A2 in Appendix A). However, to the authors best knowledge there are only few studies on TCI model comparisons. Musa et al. [52] have compared EDM and FR-EDM to model the gaseous phase combustion in ramjet engine with swirling flow. According to their paper, both TCI models predicts similar results; however, FR-EDM is preferred in such combustors with non-premixed flames. Emami et al. [53] have investigated the effect of EDM and EDC on behavior of a laboratory-scale hydrogen-fueled, dual-stage high-velocity oxy-fuel (HVOF) and reported superiority of EDC model over EDM. Using EDM, they have reported an over heat of the flow and extra release of heat near the fuel rich region (equivalence ration = 1.4); however, this over prediction is reported to be minor for leaner mixture (equivalence ration = 1). The same temperature overestimation by EDM is reported by other researchers [54–57]. In another interesting research, Parente et al. [58] have studied the application of FR-EDM and EDC using experimental and numerical analysis for an industrial burner. They reported that FR-EDM model is unable to capture the main features of the MILD reaction zone while EDC model, with detail chemical mechanism, performs satisfactorily. Like EDM, FR-EDM predicts an overshoot of temperature near the flame region with rich fuel content when compared to EDC using both global and detailed mechanism. EDC eminence has been confirmed by Mularski et al. [51] by investigating the impact of chemical reaction mechanisms and TCI approaches in entrained flow coal gasifiers for three different configurations.

Ultimately the effect of radiation models are investigated. For systems involving high temperature flow, radiative heat transfer can be dominant and have a contribution as high as 95% of total heat transfer [59–61]. This means in high temperature applications, the effect of radiative heat transfer cannot be neglected and must be taken into the account during numerical calculations. The main reason is the fact that the rates at which thermal energy is transferred by conduction and convection, are known to be approximately proportional to the temperature difference between hot and cold medium. However, the rate of thermal energy transferred by radiation is proportional to the same temperature difference raised to the fourth power. P1 and discrete ordinate model (DOM) are among the most common selected models in the literature as listed in Table A3 in Appendix A. To the authors best knowledge, there is only one comprehensive study on the radiation model comparison by Habibi et al. [62] for CFD simulation of a high temperature gaseous reactive flow (steam cracking furnace). To extend such comparisons, in current study the effects of Rosseland, P1, and DOM radiation model are studied.

2. Case Study: Off-Gas System of HIsarna Ironmaking

The HIsarna process is a new technology to produce liquid hot metal directly from iron ore and coal. Compared to the blast furnace route, coking and iron ore agglomeration (sintering and pelletizing) processes are eliminated, which inherently leads to at least 20% reduction in CO_2 emission. Further CO_2 reduction up to 80% can be achieved by incorporating carbon capture and storage (CCS) technologies.

The produced off-gas from the reduction reactions in the main reactor contains a certain amount of CO-H_2 mixture and carbon particles which need to be removed before exhausting it into the environment. Figure 2 depicts a schematic of the HIsarna main reactor and off-gas system. It consists of four parts namely “Reflux chamber”, “Air quench”, “Up leg”, and “Down leg”. Reflux chamber is a slightly angled horizontal pipe with two bends and in fact, it can be considered as a post combustion chamber for the HIsarna process. It operates at high temperatures to combust the remaining CO, H_2, and carbon particles escaping the main reactor via pure oxygen injection.

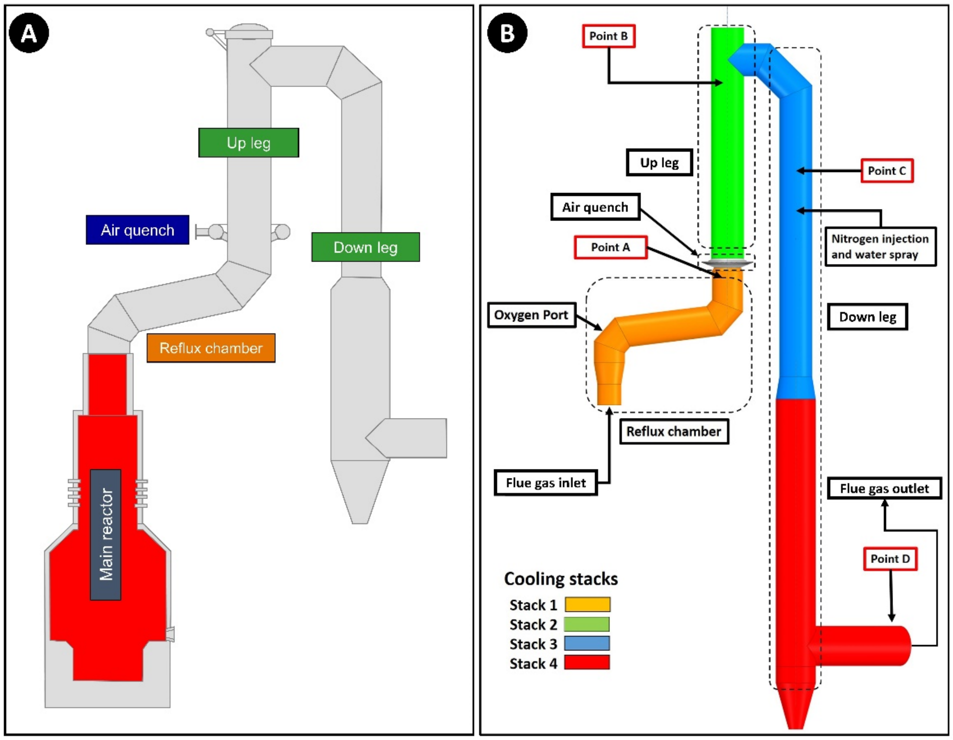

Figure 2. A: Schematic representation of HIsarna main components; main reactor and off-gas system (**A**); off-gas system with plant measurement points (**B**) (Point A: reflux chamber outlet, Point B: end of up leg, Point C: 3 m above water quench atomizers, Point D: exit to gas cooler).

Above the chamber, there is an air quench system, consisting of tilted square channels to inject air for further cooling of the flue gas. In most cases, extra cooling is achieved via nitrogen and water spray injection (evaporative cooling) in down leg. Ultimately the flue gas enters the gas cooler (Point D) to reach a proper temperature for bag house and sulfur removal unit.

3. Governing Equation

The employed governing equations for current case study are listed in Table 1. In any CFD model, solving continuity (1) and momentum (2) equations are necessary to obtain pressure, velocity, and density field.

Table 1. Governing equations and sub-models for CFD modelling of HIsarna off-gas system.

		Main Equation	Sub-Equations and Constants
Continuity equation	(1)	$\frac{\partial}{\partial t}(\rho)+\frac{\partial}{\partial x_i}(\rho\overline{u_i})=0$	
Momentum equation	(2)	$\frac{\partial}{\partial t}(\rho\overline{u_i})+\frac{\partial}{\partial x_j}\left(\rho\overline{u_i}\overline{u_j}\right)=-\frac{\partial p}{\partial x_i}+\frac{\partial}{\partial x_j}\left[\mu\left(\frac{\partial\overline{u_i}}{\partial x_j}+\frac{\partial\overline{u_j}}{\partial x_i}-\frac{2}{3}\delta_{ij}\frac{\partial\overline{u_l}}{\partial x_l}\right)\right]+\frac{\partial}{\partial x_j}(-\rho\overline{u_i'u_j'})$	$\frac{\partial\overline{u_l}}{\partial x_l}=\nabla.\overline{u}.IM$ $\overline{u}=u-u'$ $\rho\overline{u_i'u_j'}=-\mu_t\left(\frac{\partial\overline{u_i}}{\partial x_j}+\frac{\partial\overline{u_j}}{\partial x_i}\right)+\frac{2}{3}\left(\rho k+\mu_t\frac{\partial\overline{u_l}}{\partial x_i}\right)\delta_{ij}$
Turbulence models		Realizable k-ε Model Equation for turbulent kinetic energy (k)	
	(3)	$\frac{\partial}{\partial t}(\rho k)+\frac{\partial}{\partial x_i}(\rho k\overline{u_i})=\frac{\partial}{\partial x_j}\left[\left(\mu+\frac{\mu_t}{\sigma_k}\right)\frac{\partial k}{\partial x_j}\right]+G_k+G_b-\rho\varepsilon-Y_M+S_k$	$\mu_t=\rho C_\mu\frac{k^2}{\varepsilon}$ $\sigma_k=1$ and $\sigma_\varepsilon=1.2$ $C_{1\varepsilon}=1.44$ $C_2=1.9$
		Equation for dissipation of turbulent kinetic energy (ε):	
	(4)	$\frac{\partial}{\partial t}(\rho\varepsilon)+\frac{\partial}{\partial x_j}\left(\rho\varepsilon\overline{u_j}\right)=\frac{\partial}{\partial x_j}\left[\left(\mu+\frac{\mu_t}{\sigma_\varepsilon}\right)\frac{\partial\varepsilon}{\partial x_j}\right]+\rho C_1S\varepsilon-\rho C_2\frac{\varepsilon^2}{k+\sqrt{\vartheta\varepsilon}}+C_{1\varepsilon}\frac{\varepsilon}{k}C_{3\varepsilon}G_b+S_\varepsilon$	
		SST k-ω model Equation for turbulent kinetic energy (k)	$\mu_t=\frac{\rho k}{\omega}\frac{1}{max\left[\frac{1}{\alpha^*},\frac{Sr.F_2}{a_1\omega}\right]}$
	(5)	$\frac{\partial}{\partial t}(\rho k)+\frac{\partial}{\partial x_i}(\rho k\overline{u_i})=\frac{\partial}{\partial x_j}\left[\left(\mu+\frac{\mu_t}{\sigma_k}\right)\frac{\partial k}{\partial x_j}\right]+G_k-Y_k+S_k$	$\sigma_k=\frac{1}{F_1/\sigma_{k,1}+(1-F_1)/\sigma_{k,2}}$ $\sigma_\omega=\frac{1}{F_1/\sigma_{\omega,1}+(1-F_1)/\sigma_{\omega,2}}$
		Equation for turbulent kinetic energy dissipation rate (ω):	$F_1=\tanh\left(\phi_1^4\right)$ $F_2=\tanh\left(\phi_2^2\right)$
	(6)	$\frac{\partial}{\partial t}(\rho\omega)+\frac{\partial}{\partial x_j}\left(\rho\omega\overline{u_j}\right)=\frac{\partial}{\partial x_j}\left[\left(\mu+\frac{\mu_t}{\sigma_\omega}\right)\frac{\partial\omega}{\partial x_j}\right]+G_\omega-Y_\omega+D_\omega+S_\omega$	$\phi_2=max\left[\frac{\sqrt{k}}{0.09\omega y},\frac{500\mu}{\omega y^2\rho}\right]$ $\phi_1=min\left[max\left(\frac{\sqrt{k}}{0.09\omega y},\frac{500\mu}{\omega y^2\rho}\right),\frac{4\rho k}{\sigma_{\omega,2D_\omega^+y^2}}\right]$ $D_\omega^+=max\left[2\rho\frac{1}{\sigma_{\omega,2}\omega}\frac{\partial k}{\partial x_j}\frac{\partial\omega}{\partial x_j},10^{-10}\right]$ $\sigma_{k,1}=1.176,\sigma_{\omega,1}=2.0,\sigma_{k,2}=1.0$ $\sigma_{\omega,2}=1.168,a_1=0.31,\ \alpha^*=1$
Energy equation	(7)	$\frac{\partial}{\partial t}(\rho E)+\nabla.\left(\overline{u}(\rho E+p)\right)=\nabla.\left(k_{eff}\nabla T-\sum_j h_j\vec{J_j}+(\tau_{eff}.\overline{u})\right)+S_h$	$\vec{J_i}=-\left(\rho D_{i,m}+\frac{\mu_t}{Sc_t}\right)\nabla Y_i-D_{T,i}\frac{\nabla T}{T}$
Radiation models		Discrete ordinate model (DOM)	
	(8)	$\nabla\cdot\left(I\left(\vec{r},\vec{s}\right)\vec{s}\right)+(a+\sigma_s)I\left(\vec{r},\vec{s}\right)=an^2\frac{\sigma T^4}{\pi}+\frac{\sigma_s}{4\pi}\int_0^{4\pi}I(\vec{r},\vec{s}')\phi(\vec{s},\vec{s}')d\Omega'$	
		P1 model:	
	(9)	$q_r=-\Gamma_r\nabla G$ $\Gamma_r=\frac{1}{3(a+\sigma_s)-C\sigma_s}$	
	(10)	$\nabla.(\Gamma_r\nabla G)-\alpha G+4an^2\sigma T^4=0$	
	(11)	$-\nabla\cdot q_r=aG-4a\sigma T^4$	

		Rosseland model:	
		$\vec{q}_r = -\Gamma_r \nabla G$	
	(12)	$G = 4\sigma n^2 T^4$	
	(13)	$q_r = -16\sigma \Gamma_r n^2 T^3 \, \nabla G$	
Species transport equation	(14)	$\frac{\partial}{\partial t}(\rho Y_i) + \frac{\partial}{\partial x_i}(\rho \bar{U} Y_i) = -\nabla . \vec{J_i} + R_i + S_i$	
Turbulence-chemistry interaction models		Finite rate model (FR):	
	(15)	$R_{i-FR} = M_{w,i} \sum_{r=1}^{N_R} \hat{R}_{i,r}$	$k_{f,r} = A_r T^{\beta_r} e^{-E_r/RT}$ $k_{b,r} = \frac{k_{f,r}}{K_r}$
	(16)	$\hat{R}_{i,r} = \theta\left(v''_{i,r} - v'_{i,r}\right)\left(k_{f,r} \prod_{j=1}^{N} \left[C_{j,r}\right]^{\eta'_{j,r}} - k_{b,r} \prod_{j=1}^{N} \left[C_{j,r}\right]^{\eta''_{j,r}}\right)$	
		Eddy dissipation model (EDM):	
	(17)	$R_{i-EDM} = \frac{A\varepsilon}{k} \min\,(f_i, v_i)$	
		Finite rate eddy dissipation model (FR-EDM)	
	(18)	$R_{i-FR-EDM} = \min\,(R_{i-EDM},\ R_{i-FR})$	
		Finite rate eddy dissipation model—relaxed to equilibrium (FR-EDM-rex):	
	(19)	$R_i = \rho \frac{Y_i^{eq} - Y_i}{\tau_{char}}$	
		Eddy dissipation concept (EDC):	
	(20)	$R_i = \frac{\rho(\zeta^*)^2}{\tau^*[(1-(\zeta^*)^3)]}(Y_i^* - Y_i)$	$C_\zeta = 2.1377$ $C_\tau = 0.4082$
	(21)	$\zeta^* = C_\zeta \left(\frac{v\varepsilon}{k^2}\right)^{0.25}$	
	(22)	$\tau^* = C_\tau \left(\frac{v}{\varepsilon}\right)^{0.5}$	
Particle force balance equation—Discrete phase model	(23)	$m_p \frac{d\vec{u}_p}{dt} = m_p \frac{\vec{u} - \vec{u}_p}{\tau_r} + m_p \frac{\vec{g}(\rho_p - \rho)}{\rho_p} + \vec{F}$	
Particle evaporation model	(24)	$\frac{dm_p}{dt} = k_c A_p \rho . Ln(1 + \frac{Y_{i,s} - Y_{i,\infty}}{1 - Y_{i,s}})$	
carbon particle reaction rate	(25)	$\overline{R_{char}} = \frac{dm_c}{dt} = -A_p y_j R_{char,i}$	
	(26)	$R_{char,i} = \frac{1}{\frac{1}{k_{diff,i}} + \frac{1}{k_{s,i} Y^2} + \frac{1}{k_{dash,i}}\left(\frac{1}{Y} - 1\right)}(P_i - P_i^*)$	

The flow inside the current off-gas system is turbulent with a high Reynolds number of 51,000 at the inlet. To take into account the effect of turbulency, two different models namely k-ε and SST k-ω are considered for selection.

On the other hand, due to the high temperature nature of the flow and large temperature difference between flue gas and water-cooled walls, the effect of radiation is included in the source term of the energy equation for correct prediction of heat flux and temperature profile across the off-gas system. In Table 1, related equations for Rosseland, P1, and DOM models are reported. Among them, DOM is the most comprehensive one for which transport equation of radiation intensity (8) is solved and then included in the source term of energy Equation (7). P1 model is a relatively simpler approach for modelling radiative heat transfer. In this approach, the radiation flux (9) is written based on the incident radiation (G) and then is combined with the transport equation of incident radiation to obtain Equation (11). The final equation is basically an expression for radiation flux gradient ($\nabla \cdot q_r$) which is included in the energy Equation (7) to account for heat sources or sinks due to the radiation. In the Rosseland model, incident radiation is considered constant and equal to black body radiation (12) without solving transport equation. By substituting Equation (12) in (9), the equation for radiation flux (13) is obtained and can be included in energy equation source terms. A composition-dependent absorption coefficient model known as weighted-sum-of-gray-gases model (WSGGM), is used instead of constant absorption coefficients. See references [63–66] for more details.

The flue gas inside the off-gas system is a multi-component mixture of different gaseous species. To obtain the local mass fraction of each species, a convection-diffusion equation known as species transport Equation (14) needs to be solved. In a non-reactive flow, the term R_i (net source of chemical species due to reaction) and S_i (net rate of creation by addition from the dispersed phase like particles) in the equation are zero. However, for reactive flow it will be calculated through TCI models. In Table 1, three different TCI models are listed for comparison.

In finite rate (FR) approach [67], R_i is calculated as the sum of the Arrhenius reaction sources over the limited number of reactions as written in Equations (15) and (16). However, with FR calculations, the effect of turbulence is not taken into account. Compared to laminar flow, turbulent flow is characterized by intensive mixing properties which can strongly enhance the diffusion process and as a result the chemical reaction rate [68,69]. There has been extensive effort on developing reliable approaches to consider the effect of turbulence in reactive flows. EDM is one of the most utilized approaches [70] which assumes the chemical reactions to be faster than the transport processes. The products are instantaneously formed once the reactants are mixed and the overall rate of reaction is controlled by turbulent mixing. This way, calculation of R_i is mixing limited meaning that it is purely calculated based on the local mixing properties of the flow (turbulent kinetic energy k and its dissipation rate ε)without considering finite rate constants and kinetic data [53,55,57]. In applications where ignition is important or when chemical kinetics control the reaction rate, using EDM will lead to a poorly predicted properties. Moreover, since the effect of chemical kinetics is ignored by EDM, the effects of intermediate species and possible dissociation reactions which are endothermic are not taken into account. This will cause the over-prediction of the local temperature which is more pronounced in highly turbulent flow and fuel rich regions [53,71]. More importantly, EDM calculates the same turbulent rate for all reactions and therefore including detailed mechanism would not make any specific difference compared to global mechanism. In fact, it is better to use EDM with global mechanism [51,53,58,72].

These drawbacks can be redeemed by considering finite rate an kinetic data in EDM calculations. This combination is usually referred to as finite rate/eddy dissipation model (FR-EDM). In this approach two values for R_i are obtained; one from the FR approach and the other from EDM, and the slowest reaction rate is used. There are still some problems with this approach such as ignition initiation. This means that in some cases, the reactions are not initiated and artificial heat sources are required for reaction persistence and flame formation. One remedy to this issue would be driving the species composition to its equilibrium state according to the Equation (19). As will be discussed later, the assumption of chemical equilibrium can lead to large errors in fuel-rich zones.

On the other hand, EDC model can be utilized to include detailed chemical mechanisms in turbulent flows. The R_i term in this approach is calculated from Equation (20). In contrast to EDM and FR-EDM, EDC model provides an empirical expression for the mean reaction rate based on the assumption that chemical reactions occur in regions where dissipation of the turbulence energy takes place. These regions occupying only a small fraction of the flow consist of "fine structures" whose characteristic dimensions are of the order of Kolmogorov's length scale. The characteristic length is defined in two dimensions which appear intermittently and are not evenly distributed in time and space [73]. The length fraction (ζ^*) of the fine scales is modelled according to Equation (21). After defining the fine structure and the spaces they occupy, they are considered as perfectly stirred reactor with constant pressure in which all reactions take place over a time scale (τ^*) defined in Equation (22).

Particle behavior (carbon particles and water droplets) is modelled using the discrete phase method (DPM). The force balance equation is written in Lagrangian reference frame and trajectory of particles are calculated based on the Equation (23) and by integrating the force balance on each particle. The spherical drag force proposed by Morsi et. al. [74] is used in this study where particles are considered smooth and spherical. The dispersion of particles due to turbulence in the fluid phase can be predicted using the discrete random walk (DRW) model. The related equations for DRW model is not mentioned in this study; however, more details can be found in the study of Mofakham et al. [75]. In order to properly calculate the overall behavior of particles and also physical representation of the particle flowrate, suitable number of particles must be included in the computational domain. In DRW model, number of particles can be control by a parameter called "number of tries" (NTs). The higher the NTs, the higher is number of injected particles for a fixed particle flow rate.

Furthermore, liquid droplets evaporation is modelled using a convection/diffusion controlled sub-model as stated in Equation (24).

For carbon particle combustion, field char oxidation model is used which is a simplification of unreacted shrinking core model (USCM). The combustion rate of solid carbon is modelled using DPM multiple surface reaction model and the rate is calculated from the expressions (25) and (26). In the current calculations the effect of ash layer is neglected.

4. Base Model Set up and Validation

The base model is established, validated, and discussed in another study by the same authors [76]. In this section, a brief review on the model set up and boundary conditions are presented.

4.1. Computational Grid (Mesh)

The computational grid (mesh) is composed of polyhedral cells (2.6 million cells) with prism layers to create inflation on the walls. A representation of polyhedral computational grid for the inlet section of off-gas system is shown in Figure 3C.

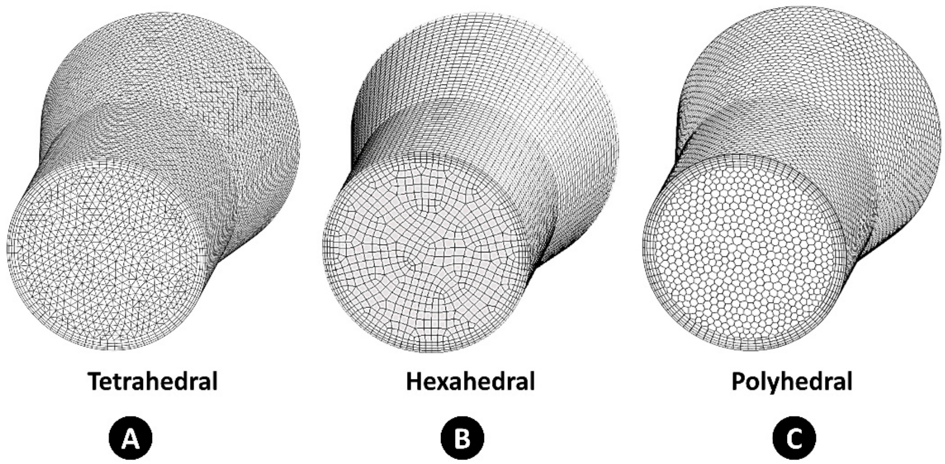

Figure 3. Different mesh cell type for off-gas system inlet region.

As will be discussed in detail later, the advantage of using polyhedral cells is lesser cell counts compared to tetra and hexahedra elements while maintaining the accuracy of the predictions. A detailed discussion on cell type and mesh sensitivity analysis is presented in Sections 5.1 and 5.2.

4.2. Boundary Conditions

The data used for boundary conditions are obtained from the HIsarna pilot plant and by averaging over a fixed operating period. All inlet conditions and compositions are listed in Table 2.

Table 2. Inlet boundary conditions for CFD model setup.

	Flue Gas Inlet	**Air Quench Inlet**	**Oxygen Port Inlet**	**Nitrogen Ports Inlet**	**Water Spray Injection**
Temperature [K]	2086	293	293	293	293
Volumetric flowrate [m^3/s]	20.8	3.10	0.206		-
Average density [Kg/m^3]	0.208	1.19	1.31	1.25	998
mass flowrate [Kg/s]	4.33	3.69	0.27	0.205	0.45
Composition—average mole fraction at inlet					
CO	0.0261	0	0	0	0
CO_2	0.61	0.0003	0	0	0
H_2	0.002	0	0	0	0
O_2	0	0.21	0.995	0	0
N_2	0.166	0.78	0.005	1	0
H_2O	0.2	0.012	0	0	1
Post Combustion Ratio [%]	96.63	-	-	-	-

The flowrate of carbon particles is considered to be 0.0282 kg/s with uniform particle size of 12×10^{-5} m. As mentioned before, particle dispersion is considered using DRW model. For carbon flow, a total of 16,000 injected particles (NTs = 20, this parameter will be discussed in details later) are considered. At current HIsarna pilot plant, the water is sprayed through a set of three blast atomizer with nitrogen as carrier gas. The water droplet diameter is modelled using cone injection with diameter of 9×10^{-5} m, injection velocity of 25 m/s, and spray angle of 30 degree. The reflux chamber walls are made of steel tubes and the inner side is covered with refractory. Above the reflux chamber, the walls are only made of steel tubes (OD: 0.038 m, thickness: 0.005 m). Water flows through the pipes and cools the wall in counter current flow. The cooling system is divided into four different cooling stacks as shown in Figure 2. To consider different layers, shell conduction approach is used for the wall modelling. The material specifications and cooling water heat transfer properties are listed in Table 3.

Table 3. Wall material and cooling water heat transfer properties for shell conduction modelling.

Parameters	**Refractory**	**Steel Pipe**	
Thermal conductivity [W/m-K]	3.65	$k = \begin{cases} 0.00025 \times \mathrm{T[K]} + 0.80175 & 1073 \le \mathrm{T} \le 1273 \\ 0.0007 \times \mathrm{T[K]} + 0.2289 & 1273 < \mathrm{T} \le 2273 \end{cases}$	
Heat Capacity [J/kg-K]	836	461	
Density [Kg/m^3]	3010	7850	
Thickness [m]	0.037	0.005	
Cooling water properties	Stack1	Stack 2 and 3	Stack 4
Average Temperature [K]	314	307	314.5
Water side heat transfer coefficient [W/m^2-K]	5000	4500	4000

4.3. Reactions and Kinetics

For volumetric reactions, the proposed mechanism by Frassoldati et al. [47], is used containing 14 species with a reasonable number of 33 reactions (Table 4).

Table 4. $CO/H_2/O_2$ mechanism with rate coefficients in the form $k = A \cdot T^n \cdot \exp^{(-Ea/RT)}$, A units: mol/L/s/K; Ea units: cal/mol; n is the temperature exponent [47].

	Reaction	**A**	**n**	**Ea**
1	$H + O_2 = OH + O$	2.21×10^{11}	0	16,650
2	$O + H_2 = OH + H$	4.33×10^{10}	0	10,000
3	$H + O_2 + [M] = HO_2 + [M]$	4.65×10^{9}	−0.8	0
4	$H + O_2 + O_2 = HO_2 + O_2$	8.90×10^{8}	0	−2822
5	$OH + HO_2 = H_2O + O_2$	5.00×10^{10}	0	1000
6	$H + HO_2 = OH + OH$	2.50×10^{11}	0	1900
7	$O + HO_2 = O_2 + OH$	3.25×10^{10}	0	0
8	$OH + OH = O + H_2O$	7.36×10^{9}	0	1100
9	$H_2 + [M] = H + H + [M]$	2.23×10^{11}	0	96,081
10	$O_2 + [M] = O + O + [M]$	1.55×10^{11}	0	115,120
11	$H + OH + [M] = H_2O + [M]$	4.50×10^{16}	−2	0
12	$H + HO_2 = H_2 + O_2$	2.50×10^{10}	0	700
13	$HO_2 + HO_2 = H_2O_2 + O_2$	2.11×10^{9}	0	0
14	$OH + OH + [M] = H_2O_2 + [M]$	7.40×10^{10}	−0.37	0
15	$O + OH + [M] = HO_2 + [M]$	1.00×10^{10}	0	0
16	$H + H_2O = H_2 + OH$	4.00×10^{7}	1	19,000
17	$H_2O_2 + H = H_2O + OH$	2.41×10^{10}	0	3970
18	$H_2O_2 + H = H_2 + HO_2$	6.03×10^{10}	0	7950
19	$HO_2 + H_2O \rightarrow H_2O_2 + OH$	5.39×10^{5}	2	28,780
20	$OH + H_2O_2 \rightarrow H_2O + HO_2$	3.20×10^{5}	2	−4170

21	$O + H_2O_2 \rightarrow OH + HO_2$	1.08×10^6	2	−1657
22	$CO + O + [M] = CO_2 + [M]$	9.64×10^7	0	3800
23	$CO + OH = CO_2 + H$	9.60×10^8	0.14	7352
24	$CO + HO_2 = CO_2 + OH$	3.01×10^{10}	0	23,000
25	$CO + H_2O = CO_2 + H_2$	2.00×10^8	0	38,000
26	$O_2 + CO = CO_2 + O$	2.53×10^9	0	47,700
27	$HCO + [M] = CO + H + [M]$	1.20×10^{14}	−1	17,000
28	$HCO + O = CO_2 + H$	3.00×10^{10}	0	0
29	$HCO + H = H_2 + CO$	1.00×10^{11}	0	0
30	$HCO + OH = H_2O + CO$	5.00×10^{10}	0	0
31	$HCO + HO_2 = H_2O_2 + CO$	4.00×10^8	0	0
32	$O_2 + HCO = HO_2 + CO$	1.00×10^9	0	0
33	$HCO + HO_2 \Rightarrow H + OH + CO_2$	3.00×10^{10}	0	0

Three different reactions are considered for carbon gasification. The kinetic expressions are taken from study of Wen et al. [77] in the form of Equations (25) and (26). The reactions and kinetic data are as follows:

$$\begin{aligned}
&\mathbf{2C(s) + O_2 \rightarrow 2CO} \qquad \Delta H_{298} = -221\ \text{kJ/mol}\\
&\mathrm{k_s} = 8710 \exp\left(-\frac{17967}{\mathrm{T_s}}\right)\\
&\mathrm{k_{diff}} = 1.383 \times 10^{-3}\left(\frac{\mathrm{T}}{1800}\right)^{0.75} / (\mathrm{P_{op}}.\,\mathrm{d_p})\\
&P_i - P_i^* = P_{O_2}
\end{aligned} \tag{27}$$

$$\begin{aligned}
&\mathbf{C(s) + CO_2 \rightarrow 2CO} \qquad \Delta H_{298} = +172\ \text{kJ/mol}\\
&k_s = 247\, exp\left(-\frac{21060}{T_s}\right)\\
&k_{diff} = 7.45 \times 10^{-4}\left(\frac{T}{2000}\right)^{0.75} / (P_{op}.\, d_p)\\
&P_i - P_i^* = P_{CO_2}
\end{aligned} \tag{28}$$

$$\begin{aligned}
&\mathbf{C(s) + H_2O \rightarrow CO + H_2} \qquad \Delta H_{298} = +131\ \text{kJ/mol}\\
&k_s = 247 \exp\left(-\frac{21060}{T_s}\right)\\
&k_{diff} = 1 \times 10^{-4}\left(\frac{T}{2000}\right)^{0.75} / (P_{op}.\, d_p)\\
&P_i - P_i^* = P_{H_2O}
\end{aligned} \tag{29}$$

In above expressions, $T = (\mathrm{Tg} + \mathrm{Tp})/2$ and for simplification, the ash layer influence on combustion is neglected and the combustible fraction of carbon particles is set to 99%. The above parameters lead to an overall rate with unit of $\frac{g}{cm^2\, s\, atm}$. Proper unit conversions are performed and expressions can be implemented through either user-defined function (UDF) or as Arrheniusian direct input according to Table 5.

Table 5. Kinetic data for carbon gasification as direct Ansys Fluent input.

Reaction	A	E [J/kgmol]	Temperature Exponent	Diffusion Rate Constant []
$\mathbf{2C(s) + O_2 \rightarrow 2CO}$	0.85961	1.49378×10^{8}	1	4.94×10^{-12}
$\mathbf{C(s) + CO_2 \rightarrow 2CO}$	0.02438	1.75093×10^{8}	0	2.4584×10^{-12}
$\mathbf{C(s) + H_2O \rightarrow CO + H_2}$	0.02438	1.75093×10^{8}	0	3.3×10^{-13}

4.4. Model Solution Procedure

Ansys Fluent® 19.0 commercial software, which is a CFD code solver based on finite volume method, is used to solve and couple the governing equations. Table 6 summarizes the main models and sub-models selected for the development of the base model. Pseudo transient coupled scheme is used for pressure-velocity coupling with pseudo time step of 10^{-4}. Numerical discretization of conservation and transport equations are performed using the second-order upwind scheme. Ultimately a convergence criterion of 10^{-4} for the relative error between two successive iterations is specified. The numerical calculations were performed on a workstation equipped with Intel Xeon, 3.4 GHz CPU and 64 GB of RAM and in parallel mode using 12 out of 24 available logical processors.

Table 6. Selected sub-models for the base model.

Sub Models	Model/Algorithm
Turbulent flow	Realizable k-ε model Enhanced wall treatment
TCI	EDC
Radiation	DOM
Particle trajectory	DPM model with stochastic tracking
Particle dispersion (NTs)	DRW model (20)
Gas solid reaction	DPM multiple surface reaction model Field char oxidation
Particle evaporation	Convection-diffusion

4.5. Base Model Validation

Figure 4 shows the temperature and composition profile along the off-gas system. The length axis refers to the length of a line passing through the center of the off-gas geometry. The calculated temperature and compositions are averaged on a cross section sweeping along the mentioned line. As it can be seen that the model predictions (solid lines) are in good agreement with plant measured values (symbols).

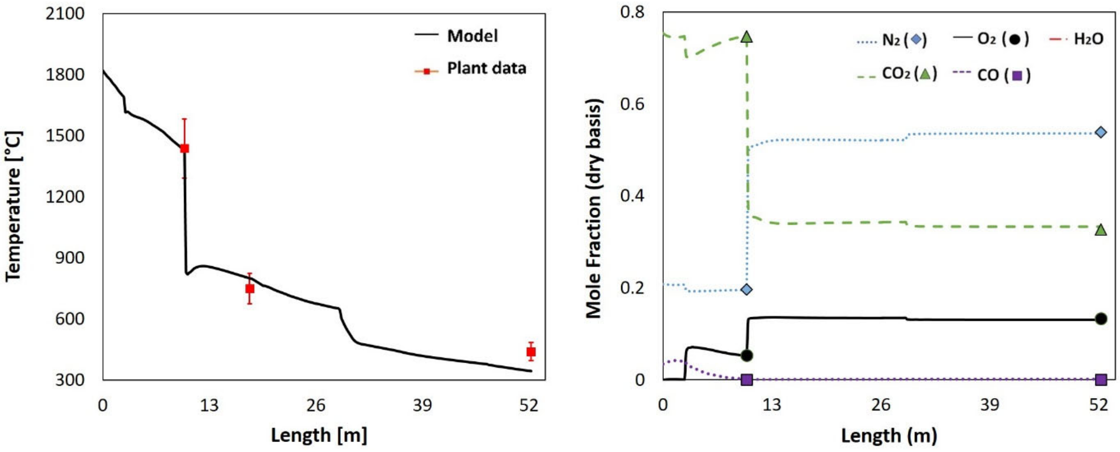

Figure 4. Calculated off-gas composition and temperature profile—model predictions (solid lines) and plant measured values (symbolled points).

The calculated heat loss through the walls in MW are 3.92 (measured: 3.9; error: 0.5%), 4.85 (measured: 5.4; error: 10%), and 8.7 (measured: 9.3; error: 6.5%) for reflux chamber, rest of the off-gas system, and the whole off-gas system respectively. The developed model is used to investigate the different parameters in pilot scale and results are discussed in details in another studies [76].

5. Result and Discussion

The base model is used to investigate the effect of mesh type and size, and other submodels that have been discussed in Section 3. The analysis and comparisons are performed either for the reflux chamber (up to the length = 10 m) or up to the Point C (up to the length = 26 m) shown in Figure 2.

5.1. Effect of Mesh Cell Type

In this section, quality of the grid, number of cells and accuracy of the results are compared for two different common cell types using reflux chamber geometry.

Two different grids with the same cell size (40 mm) is generated using tetrahedral and polyhedral cells as previously shown in Figure 3. Due to the presence of sharp edges and relatively complex geometry of the off-gas system, generation of hexahedral or structured mesh was quite complex which ultimately led to a poor quality mesh. Therefore hexahedral/structural mesh grid is omitted for comparisons.

Figure 5A shows the cell count for each cell type and as it can be seen, with the same cell size, tetrahedral cells lead to noticeably higher cell count compared to polyhedral cells. The same conclusion is reported in other studies [5,33]. Moreover, applying polyhedral cell allows the flexibility of an unstructured mesh to be applied to a complex geometry without the computational overheads associated with large tetrahedral grid cell count [11].

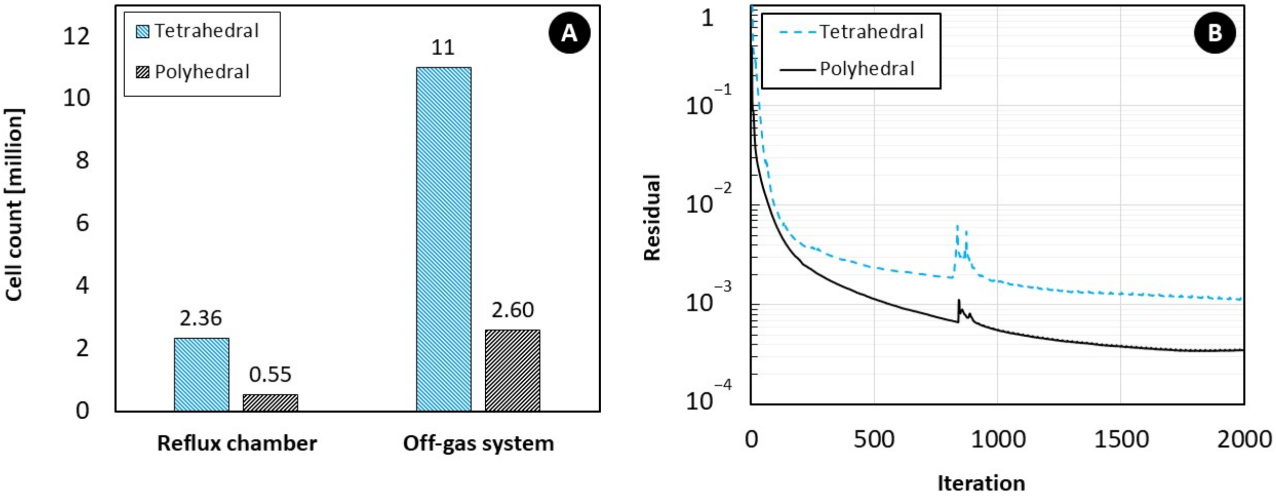

Figure 5. Cell count (**A**) and residuals (**B**) for different cell type.

On top of that, polyhedral cells increases the mesh quality which ultimately increases the calculation accuracy [13]. In order to evaluate a mesh quality, different indicators can be defined. Among them, orthogonal quality and skewness are the most important quality indicators that must be checked before proceeding to the model set up and simulations.

The concept of skewness is not applicable to polyhedral mesh; however, any polyhedral mesh have substantially lower skewness than its equivalent tetrahedral grid.

Figure 6 shows the skewness and orthogonal quality contour in the mid-plane of the reflux chamber. As illustrated, tetrahedral grid exhibits rather lower orthogonal quality compared to the polyhedral grid as reported in Table 7. High skewness and low orthogonal quality will reduce the accuracy of the interpolations on the cell surfaces which will increase the gradient errors during the calculations [5].

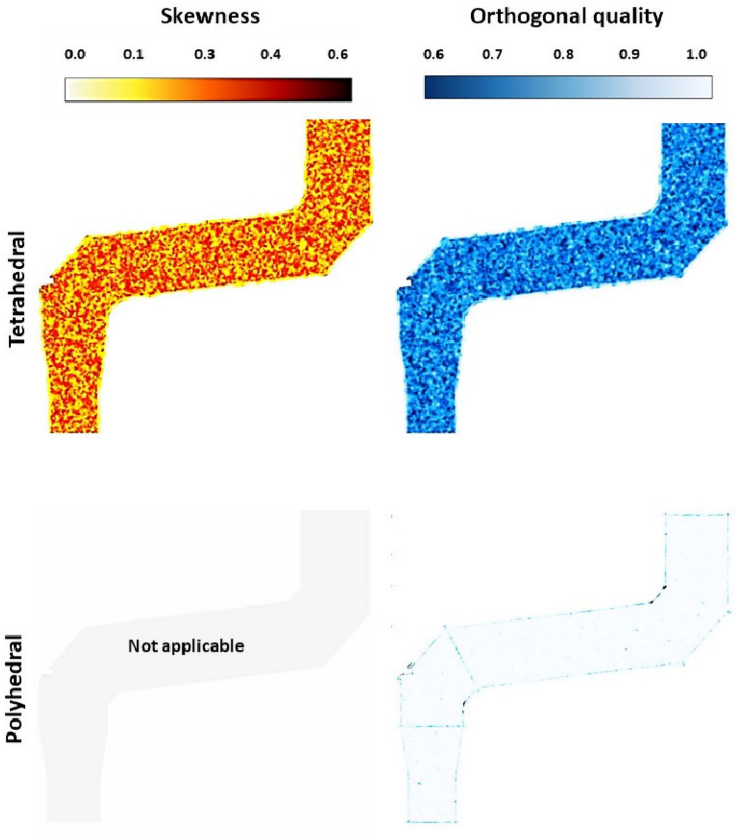

Figure 6. Skewness and orthogonal quality contours.

Table 7. Averaged skewness and orthogonal quality for reflux chamber volume.

	Tetrahedral	**Polyhedral**
Orthogonal quality	0.7891	0.9725
Skewness	0.21	-

It is possible to reduce the skewness by increasing the cell count; however it will come at the cost of increased simulation time. For both cell types, low orthogonal quality was observed near the walls and curves which can be associated to the presence of sharp and curved edges. Existing sharp edges lead to the difficulties in maintaining high mesh quality especially with prism layers. The same observation is reported in the study of Wang et al. [78]. Nevertheless, for current case, both generated grids have a good and acceptable quality for CFD calculations.

A quick CFD analysis is performed to investigate the accuracy and required simulation time for each generated grid. Figure 5B shows the continuity residuals during steady state iterations for different cell types. The simulations were performed for 2000 iteration and particles are injected at iteration 820 which led to a small spike and instability in the residuals. As depicted, polyhedral grid is converged to the set value of 10^{-4} after 2000 iterations, while tetrahedral mesh still need more iteration to reach the set convergence criteria.

Considering residual value of 10^{-3}, polyhedral grid satisfies this criteria after 570 iteration while the convergence is met after 2000 iteration for tetrahedral grid. These findings indicate higher stability of polyhedral cells due to the fact that polyhedral cells have higher number of faces and therefore more neighboring cells leading to a lower calculated gradient between cells. On the other hand, since polyhedral cells allows interchange of mass over a larger number of faces, numerical diffusion effects caused by non- perpendicular flow on cell faces is reduced specifically in a flow fields where no prevailing flow direction can be identified [12].

The other disadvantage of tetrahedral grid is longer simulation time (due to higher number of cells) which is depicted as normalized time in Figure 7. As illustrated, polyhedral grid shows noticeably lower simulation time compared to the tetrahedral grid for both total and DPM iterations time.

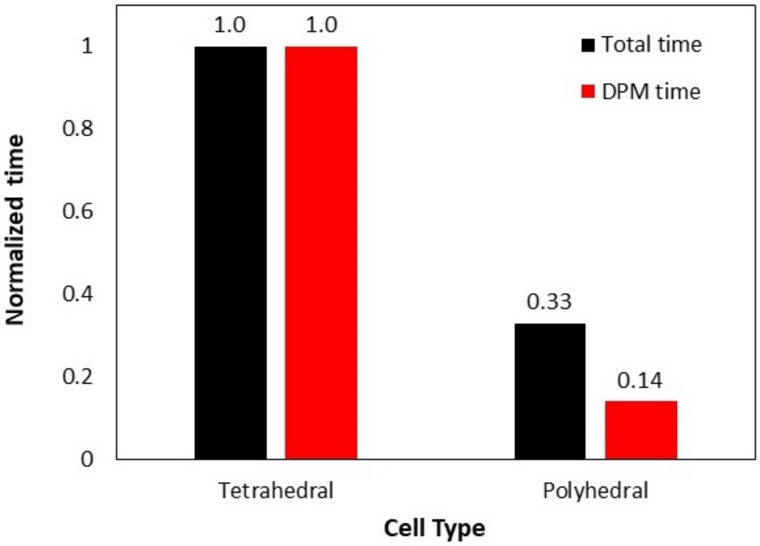

Figure 7. Simulation time for different cell type.

Figure 8 shows the predicted temperature and CO compostion profile along the reflux chmaber. As can be seen, both grids predicts more or less the same profiles with an outlet temprature quite close to the plant measurement. The carbon conversions for tetrahedral and polyhedral grid at the outlet of the chamber are 56% and 54%, respectively (plant measuremnt is 50%).

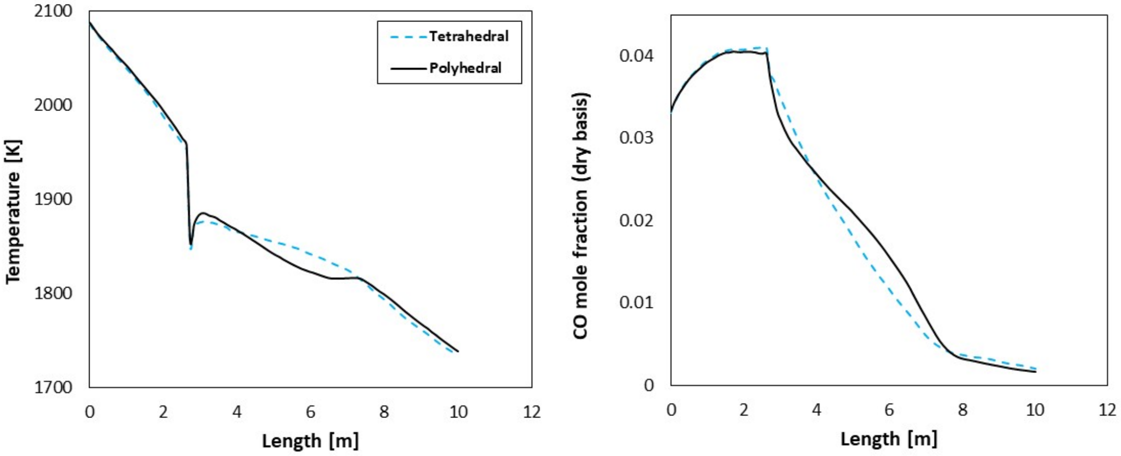

Figure 8. Predictions of different cell types for off-gas temperature and CO model fraction profile.

Altogether, the performed analysis shows that polyhedral cells hold a great promise in producing equivalent accuracy results compared to tetrahedral mesh with the added benefits of lower cell count (the most economical), faster converge with fewer iterations, convergence to lower residual values, and lower solution run-time.

5.2. Effect of Mesh Cell Count (Grid Independency Analysis for Polyhedral Cells)

Apart from the cell type, cell number constituting the mesh grid plays a crucial role in generating an optimal grid to ensure the accuracy and economic feasibility of a CFD analysis [1]. A coarse grid can yield inaccurate results and instability in analyses; therefore, it is important to use a sufficiently refined grid to ensure the adequacy of the calculations. Moreover, in any CFD calculation, one must make sure that the obtained solution is grid independent. This means that a numerical solution tends toward a unique value as grid density is increased. A solution is said to be grid independent when further grid refinement produces a negligible change in the solution.

Based on this definition, for the current case, five different polyhedral cell sizes are selected (as reported in Table 8) and simulations with the same setting as discussed for base model are performed for each grid.

Table 8. Mesh specification for mesh sensitivity analysis.

	Cell Size [mm]			**Cell Count [Million]**
Zone	**Reflux Chamber**	**Air Quench**	**Up/Down Leg**	
Very coarse	65	55	75	0.88
Coarse	55	45	65	1.05
Medium	40	30	50	2.69
Fine	30	25	40	2.3
Very fine	25	20	35	3.3

Figure 9 shows the calculated temperature and composition profile for each grid refinement. As it is evident, medium, fine, and very fine grids show the same accuracy; however coarse grids show a slight deviation with respect to medium and fine grids. The discrepancies are mainly observed in the reflux chamber where oxygen is injected (between length of 3 to 10 m). It is an important region where most of the oxidation reactions occur. Nevertheless, the solution seems to be grid independent after coarse grid. Hence for the base model and rest of the analysis, medium size grid is used since finer grids require substantially higher simulation time for the same obtained accuracy.

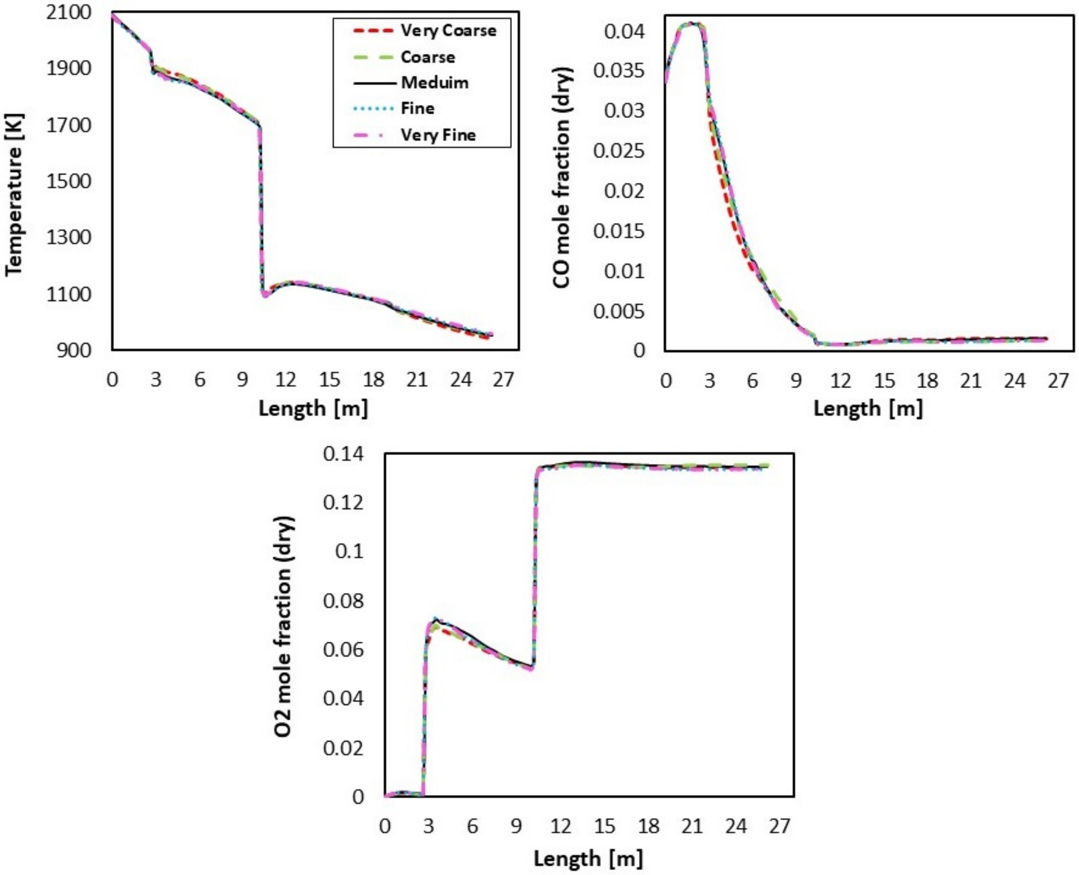

Figure 9. Off-gas temperature, CO and O_2 composition profile prediction for different polyhedral mesh refinements.

5.3. Selection of Turbulence Model

For industrial cases, k-ε and k-ω are among the most common models to describe the turbulence nature of the flow. Both models can take into account the turbulence parameter to a great accuracy. In this section, the intention is not to compare the accuracy of predictions but rather pointing out an issue the authors faced during the calculations.

Even though k-ω model is proved to be more accurate and robust in capturing the details of turbulent flows, for final model development in this study, k-ε is preferred for two main reasons.

The first and main reason is higher number of cells required by k-ω model. To correctly predict the velocity profile and subsequent thermal properties using k-ω model, a $y^+ \leq 1$ near the walls must be maintained during the calculations. Low y^+ requires higher grid resolution and more inflation layer near the wall region and consequently higher cell count. Depending on the computational resources, this could be a great disadvantage when it comes to industrial applications where geometries are usually large. However, for k-ε model, a y^+ value above 30 and up to 300 needs to be maintained which requires much coarser grid resolution near the wall regions. Indeed k-ε models use wall functions to correlate the profiles near the walls. For standard wall function, one should make sure the y^+ is either below 5 or above 30 to avoid putting the first cell in buffer region. For enhanced wall treatment, a y^+ value of either lower than 2 or higher than 30 is required. It is worth mentioning that all wall functions predict similar results for $y^+ > 30$. Nevertheless, enhanced wall treatment function, is quite y^+ insensitive and can still predict near wall region properties with a great accuracy for any y^+ values.

Beside mesh resolution there is another problem which was raised with regard to using k-ω model. To our best knowledge, the faced issue while choosing turbulence models is not reported in any other literature.

When carbon particles are included in the model, the trajectories of particles are calculated in each cell. To fulfil proper trajectory calculations, the size of all cells in the grid need to be larger than the particles diameter. In other words, all cells should have enough volume to host a single particle. For a stable calculations, it is necessary to keep the cell size at least three times higher than the particles diameter, however for specific cases, larger cells might be needed.

In the current case, using k-ω model and obtaining $y^+ < 1$ led to cell layers with a size smaller than the particle diameter. Therefore, during the calculations, the solver failed to complete the trajectory calculation and removed some particles from the domain by marking them as "incomplete". Removing carbon particles from the domain causes a reduction in the initial injected flowrate of particles which ultimately can lead to a wrong prediction of carbon conversion, gaseous composition, and temperature profile especially when carbon particle flowrate is high.

Table 9 summarizes the corresponding number of incomplete particle trajectories for different generated grids with different y^+ values. It can be seen that lower y^+ values requires lower first layer thicknesses and therefore increases number of fine cells and overall cell number. For the grid with y^+ value of 34, which is used for the rest of analysis, all trajectories are calculated without any incomplete particle trajectories.

Table 9. Tracked and incomplete particle trajectory for different y^+ (regardless of turbulent model used)—particle size is fixed and equal to 0.12 mm.

Mesh	First Layer Thickness [mm]	Number of Inflation Layers	Mesh Size (Reflux Chamber)	Mesh Size (Off-Gas System)	y^+	Number of Tracked Particles	Incomplete Particles (Average)
Mesh 1	0.2	14	880×10^3	5.31×10^6	0.38	9185	880 (10%)
Mesh 2	0.3	12	840×10^3	4.8×10^6	0.6	8800	686 (8%)
Mesh 3	0.5	10	750×10^3	4.1×10^6	0.95	7600	356 (5%)
Mesh 4	1	8	645×10^3	3.58×10^6	1.9	6315	230 (4%)
Mesh 5	2	5	627×10^3	3.12×10^6	4.6	5900	117 (2%)
Mesh 6 (base model)	10	4	485×10^3	2.6×10^6	34	4516	0

To recap, using k-ε model for the current case seems to be a better choice for two reasons. It requires lower cell count as it needs higher y^+ values near the wall region and consequently cell size will be large enough for safe particle path calculations.

5.4. Effect of Reaction Mechanism

As mentioned before, reaction mechanism can be classified into two categories. Global or multi step mechanisms which have limited number of species and reactions involved; and detailed mechanism which is a set of elementary reactions forming a complex network. Based on the presented literature review, the supremacy of detailed mechanism becomes evident. Therefore, in the current study, three different detailed mechanisms namely GRI 3.0 (325 reaction with 55 species), GRI 1.2 (177 reaction with 32 species), and the proposed mechanism by Frassoldati et al. [47] (33 reactions and 14 species; see Table 4), are used for comparison. Figure 10A,B show the predicted temperature and CO mole fraction profile respectively. As it can be seen, all studied mechanisms predict the same trend for the profiles. The predicted carbon conversions at the outlet of the reflux chamber (Point A in Figure 2B) are 53%, 54%, and 52% for Frassoldati, GRI 1.2, and GRI 3.0

respectively. However, as mentioned before, higher number of reactions will lead to higher simulation cost. Figure 10C shows the normalized simulation time for all three mechanisms for the same number of iterations.

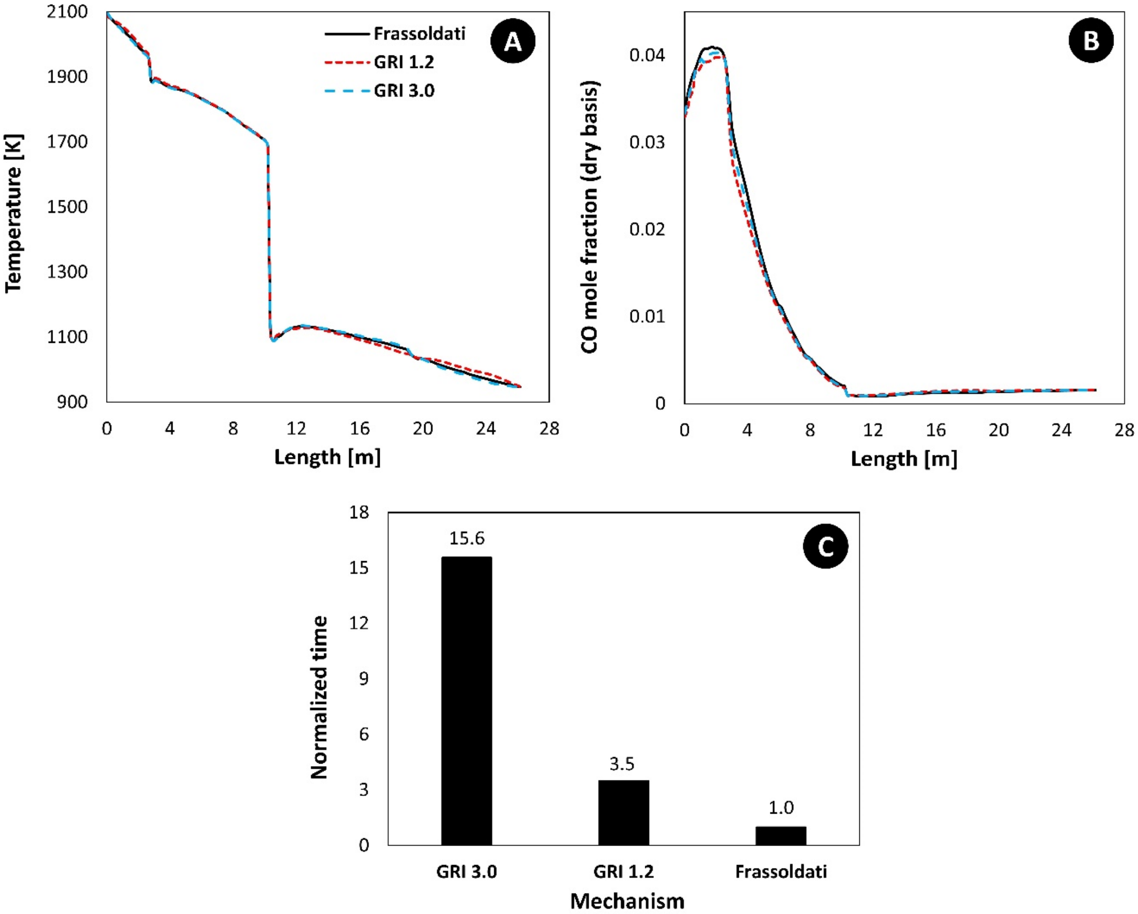

Figure 10. Predicted off-gas temperature (**A**), CO model fraction (**B**), and normalized simulation time (**C**) for different detailed mechanisms.

As it is evident, compared to GRI 3.0 and GRI 1.2, Frassoldati mechanism takes lesser simulation time by factor of 15.6 and 3.5 respectively while obtaining a similar predicted profile and carbon conversion. According to these results, the computational costs grows exponentially by increasing the number of reactions in the mechanisms therefore, utilizing detailed mechanism of Frassoldati seems to be more reasonable.

5.5. Effect of Turbulent-Chemistry Interaction Models

Among the available TCI models, eddy dissipation model (EDM), finite rate eddy dissipation model (FR-EDM), relaxed to equilibrium finite rate eddy dissipation model (FR-EDM-rex), and eddy dissipation concept model (EDC) are considered for comparison. All of the mentioned models are extension of EDM. Detailed mathematical formulation of each model has been discussed in Section 3. Since the gas–solid reactions are modelled using multiple surface reaction approach, the application of EDM is not possible and is omitted from the comparisons. To begin the comparisons, the simulations were performed using FR-EDM with detailed mechanism. However, the reactions were not initiated during calculations and all kinetic rates were estimated to be zero. This is actually one of the shortcomings of both EDM and FR-EDM that may fail to correctly predict the ignition process as mentioned earlier. The same issue is reported by Sripriya et al. [79] for post combustion of CO-H_2 mixture. To resolve this issue, they have included artificial heat source points inside the computational domain as source terms. These terms act like ignition sources to guarantee the persistence of the reactions and flame formation (if there is any). In the current study, the problem of the reaction initiation is resolved by using FR-EDM and then relaxing the calculated composition to their chemical equilibrium (FR-EDM-rex). Using this approach, the ignition is initiated without including artificial heat sources. Figure 11A shows the predicted temperature and CO mole fraction profile for EDC and FR-EDM-rex (other sub-models are the same for both TCI models).

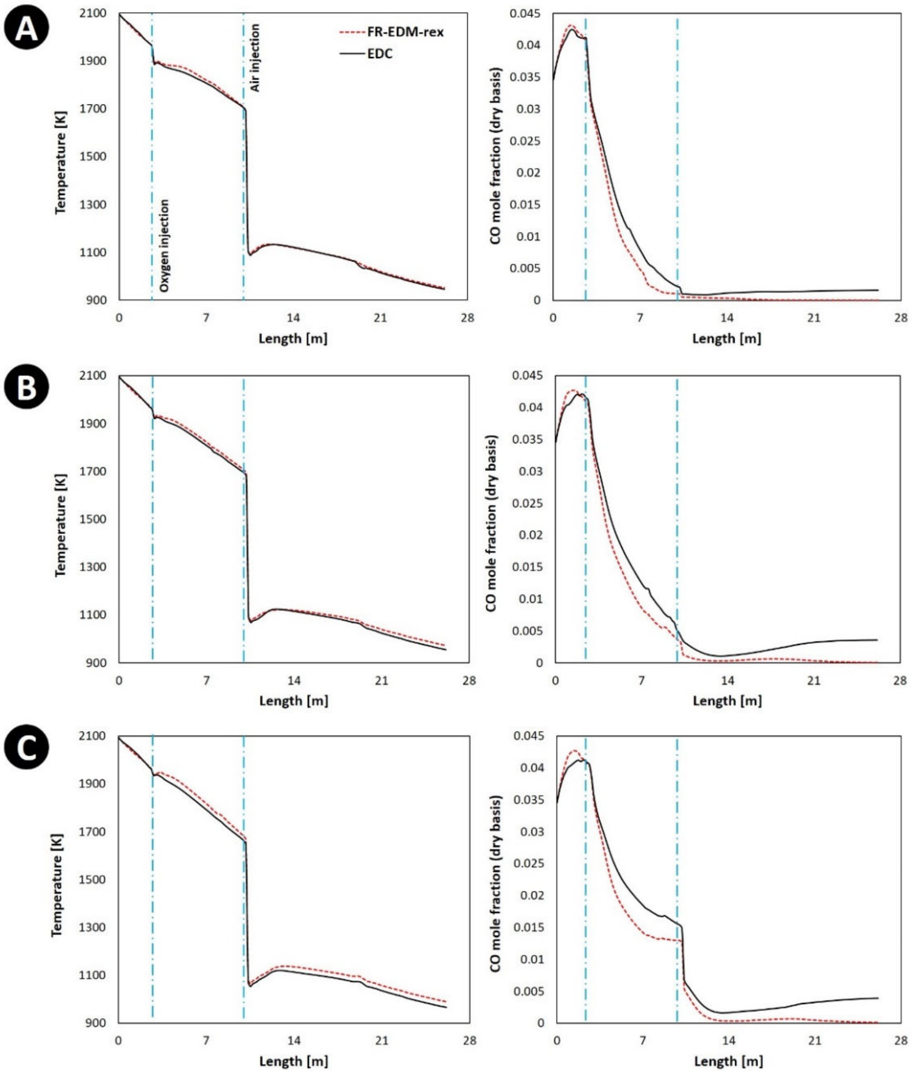

Figure 11. Comparison between FR-EDM-rex and EDC model; off-gas temperature and CO mole fraction profile for different oxygen reduction cases; (**A**) 0% reduction, (**B**) 60% redution, (**C**) 80% reduction.

As illustrated, the predictions for both models are quite similar. The similarity of predictions between TCI models have been previously reported by Rebola et al. [72] which made an assessment of the performance of several turbulence and combustion models in the numerical simulation of a flameless combustor. In another study, Chen et al. [19] have reported a similar and comparable prediction of temperature contours by EDM, FR-EDM, and EDC models. However, they have chosen EDC for further investigation of their case study.

Even though the profiles are similar, FR-EDM-rex predicts slightly higher temperature in oxygen injection region of the reflux chamber where CO-H_2 combustion takes place. A more pronounced discrepancy can be seen for CO profile in the same region where FR-EDM-rex predict lower CO mole fraction (higher CO conversion). This means that higher reaction rate is predicted by FR-EDM-rex which has been reported by other reviewed studies [53–58]

In order to have a better analysis, a set simulation was performed by creating a fuel-rich environment inside the reflux chamber. To fulfil that, the oxygen injection is reduced by 60% and 80% (injected flow rate of 0.108 and 0.054 kg/s respectively). In this condition, the discrepancies between TCI models become more evident as depicted in Figure 11B,C for 60% and 80% oxygen reduction respectively. Again, FR-EDM-rex predicts higher reaction rates, lower CO mole fraction and slightly higher temperature along the off-gas system length compared to EDC. The discrepancies in CO prediction profile is more pronounced in upleg/downleg region of off-gas system where a full combustion of CO (escaped from reflux chamber or generated by escaped carbon gasification) is predicted by FR-EDM-rex. On the contrary, EDC predicts almost no combustion, rather an increase in CO content due to the conversion of the remaining carbon content in the flow.

The discrepancies between two models can also be seen in Figure 12 where temperature, carbon conversion, and CO amount at the outlet of the reflux chamber are shown. Even though the difference in temperature and carbon conversion is minor, the models predict CO composition quite differently for fuel-rich cases.

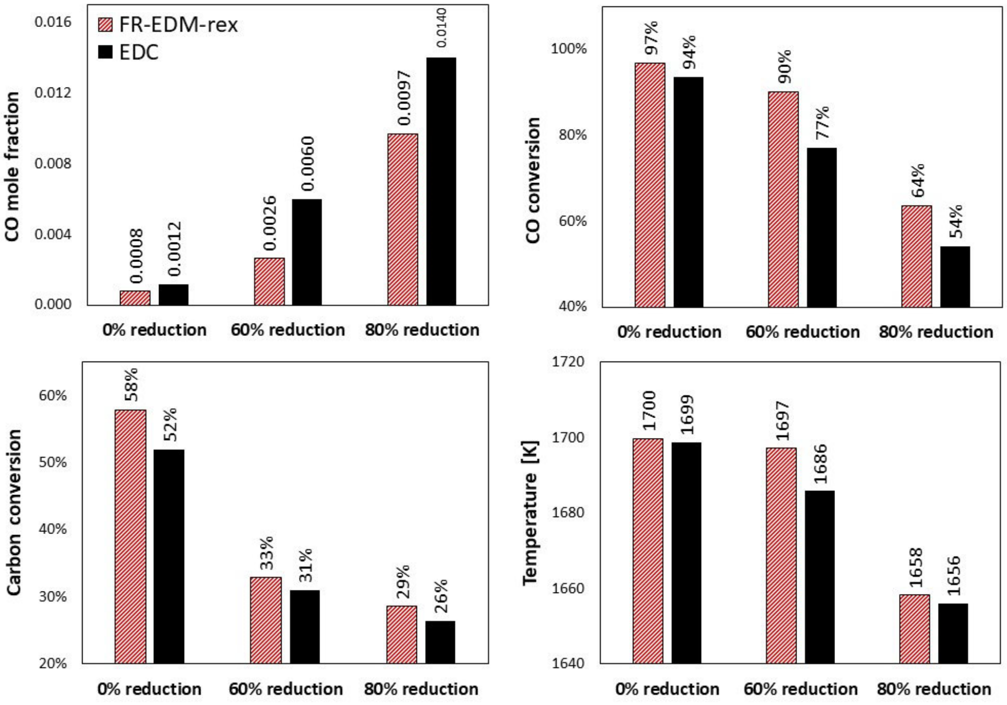

Figure 12. Comparison between FR-EDM-rex and EDC model; reflux chamber off-gas outlet temperature, CO mole fraction, CO conversion, and carbon conversion for different oxygen reduction cases.

Nevertheless, for the current case, FR-EDM-rex and EDC predict quite similar temperature, composition, and carbon conversion profile for fuel lean mixture. From the literature review and performed analysis for the current case, the following can be deduced regarding TCI model selection:

- EDM and FR-EDM are better to be used with global mechanism (with few steps) as the mixing rate is considered to be the same for all included reactions.
- FR-EDM takes into the account the effect of finite rate chemistry; however, it still predicts temperature overshoot in fuel-rich zones.
- Using FR-EDM, the ignition of reactions might be poorly predicted and the reactions might not be initiated even at very high temperatures. An artificial ignition source might be required to initiate the reaction chain.
- The performance of FR-EDM can be improved by considering relaxed to equilibrium calculation.
- For fuel lean mixture, FR-EDM-rex and EDC predict similar results with a slight difference. The discrepancies between the two appear for fuel-rich mixtures.

5.6. Effect of Gas-Solid (Carbon Particles) Reaction and Carbon Particle Dispersion

Incorporating carbon combustion reactions in the model will change the temperature and composition profile compared to a case where gas–solid reactions are excluded. Carbon particles will go through gasification reactions to generate CO and H_2 which could affect the local composition profile. The produced compounds will combust with oxygen and generate higher heat (therefore higher temperature). Figure 13 shows the effect of carbon incorporation on temperature and composition profile based on our previous study [76]. As it can be seen, both temperature and composition profiles are affected by considering carbon particle reactions.

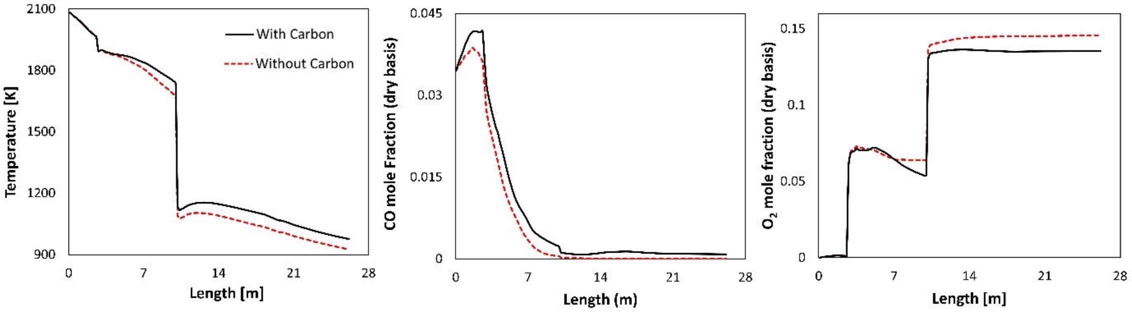

Figure 13. Effect of gas–solid (carbon) reaction on averaged cross-section composition and temperature profiles of the off-gas [76].

The effect is more pronounced by comparing O_2 profiles since including carbon particles and gasification reactions consumes higher amount of oxygen. Ultimately a better fit with industrial measurements was observed by including carbon reactions in the mechanism. Despite these benefit, incorporating gas–solid reactions using DPM model can significantly increase the calculation time. For example, for the current case, DPM calculation time is around 30% of the total calculation time to reach a convergence of 10^{-4}. Nevertheless, DPM calculation time depends on the number of injected particles which can be controlled by manipulating NTs parameter in DRW model. A sensitivity analysis is required to set minimum required particles that can precisely represent the actual particle flow.

Table 10 shows the effect of NTs on different calculated parameters (for base model and the whole off-gas geometry) which are compared to their counterpart measured values.

Table 10. Effect of NTs on predicated values.

	Plant Measurement	Calculated				
Number of tries []	**-**	1	3	5	10	20
Number of injected particles []	-	923	2769	4615	9230	15,840
Reflux chamber outlet carbon flowrate [kg/s]	-	0.0141	0.0137	0.0136	0.0135	0.0135
Reflux chamber outlet carbon conversion [%]	50	50	52	52	53	52
Reflux chamber outlet temperature [K]	1710	1692	1698	1702	1695	1702.4
Reflux chamber outlet molar composition (dry basis)						
CO	0.00	0.002	0.0021	0.002	0.00192	0.002
O_2	0.054	0.0535	0.0532	0.0534	0.0533	0.0534
Heat loss						
Reflux chamber [MW]	3.9	3.89	3.91	3.91	3.92	3.91
Rest of the off-gas system [MW]	5.4	4.87	4.85	4.87	4.83	4.83

For a better visualization, Figure 14 shows the reflux chamber outlet oxygen, temperature, and also carbon conversion for different NTs. As it can be deduced, after NTs = 5, the calculated values are roughly the same and the current case study appeared to be NTs insensitive.

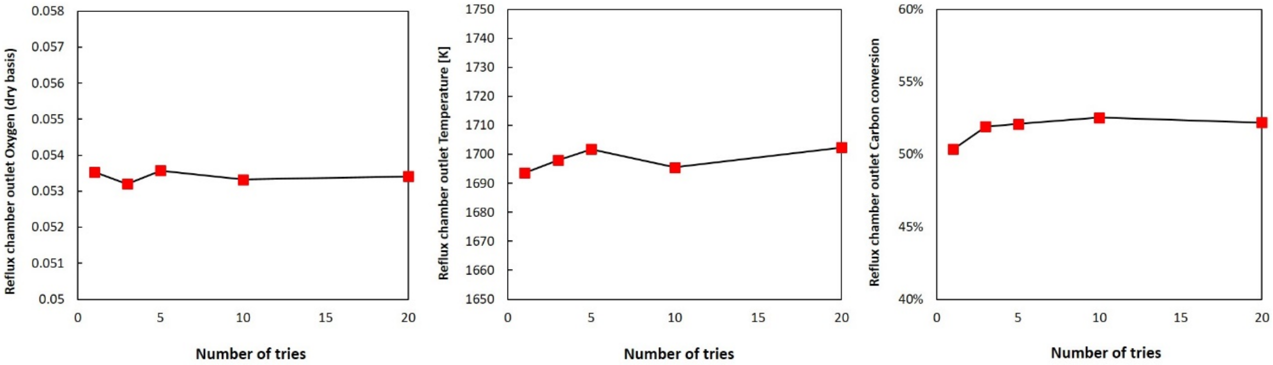

Figure 14. Predicted reflux chamber outlet values for different NTs.

Nevertheless, higher NTs can always generate more reliable results as higher number of particles are injected to represent the actual flowrate of the particles. However, higher NTs come at a higher computational cost. Figure 15 shows the normalized simulation time (normalized over the longest simulation time) for variable NTs. As it can be deduced from the graph, the simulation time grows exponentially, though with a low rate.

In cases where the computational resources are limited, it is suggested to perform a sensitivity analysis to investigate the possible reduction in NTs and therefore computational costs. It is worth reiterating that for validation of the base model, NTs of 20 is considered in this study.

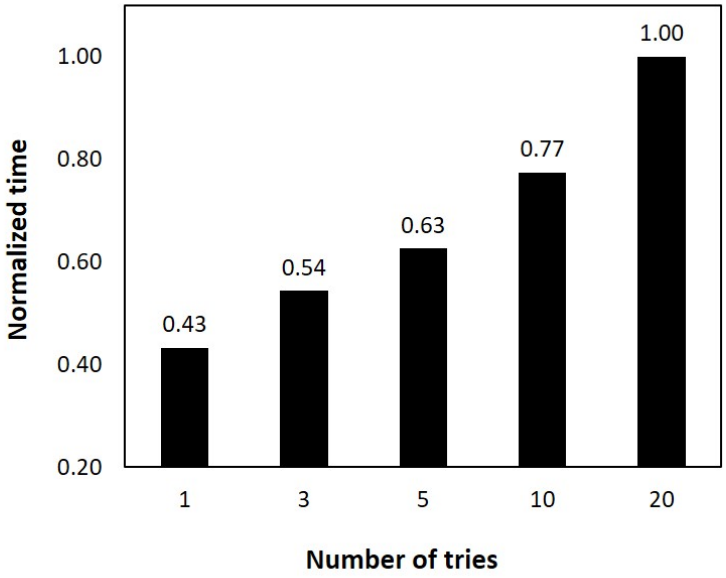

Figure 15. Normalized simulation time for different NTs.

5.7. Effect of Radiation Model

The temperature at the inlet of off-gas system could sometimes reach as high as 2200 K. The flow temperature can locally increase at the oxygen injection zone (as high as 2600 K) due to the exothermic reactions. Thus, the radiative heat transfer plays an important role [80].

In this section, four different cases are considered to compare the radiation effect inside the reflux chamber (only reflux chamber geometry is modelled). In three of the cases, Rosseland, P1, and DOM radiation models are used to take into account the radiation effect and one case is set up without any radiation model.

There are different criteria to choose a proper radiation model. The most reliable approach is comparison method, where different radiation models are used and results are compared with the measured counterparts. In the absence of proper measurements, there are still some rules of thumb for radiation model selection. A good indicator is the use of optical thickness or opacity of the medium fluid (in the current case hot flue gas). Optical thickness can be calculated according to Habibi et al. [62]:

$$\text{optical thickness} = a.Ls \ \ [\text{m}]$$

where a is absorption coefficient and the characteristic length scale $Ls = \frac{k^{1.5}}{\varepsilon}$ is length scale based on the turbulent parameter of the k-ε model. The length scale could also be the dimeter of the chamber. The larger the optical thickness, the smaller is the amount of transmitted radiative heat through the flue gas and the medium is said to be opaque or optically thick. P1 model should typically be used for optical thicknesses > 1 [62,81,82]. For optical thickness > 3, the Rosseland model is computationally cheaper and more efficient. On the other hand, DOM works across all ranges of optical thicknesses, but it is computationally more expensive than P1 and Rosseland models [83]. The calculation of this parameter for different radiation model will be discussed later. Figures 16 and 17 show the predicted temperature contour and averaged cross-sectional temperature along the reflux chamber length for different studied cases.

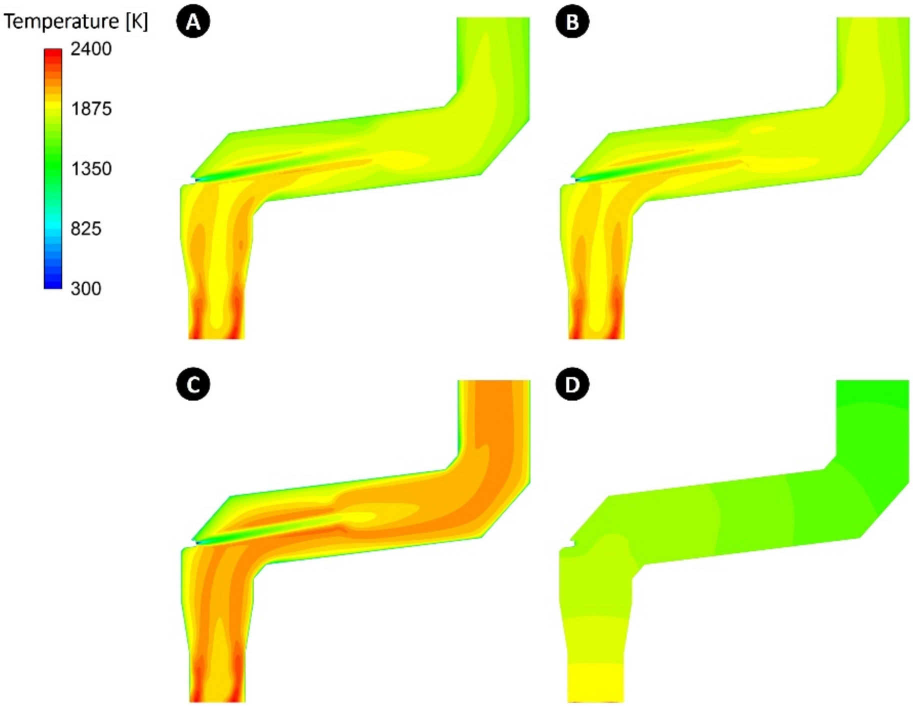

Figure 16. Predicted contour of temperature for DOM (**A**), P1 (**B**), no radiation (**C**), and Rosseland (**D**) model.

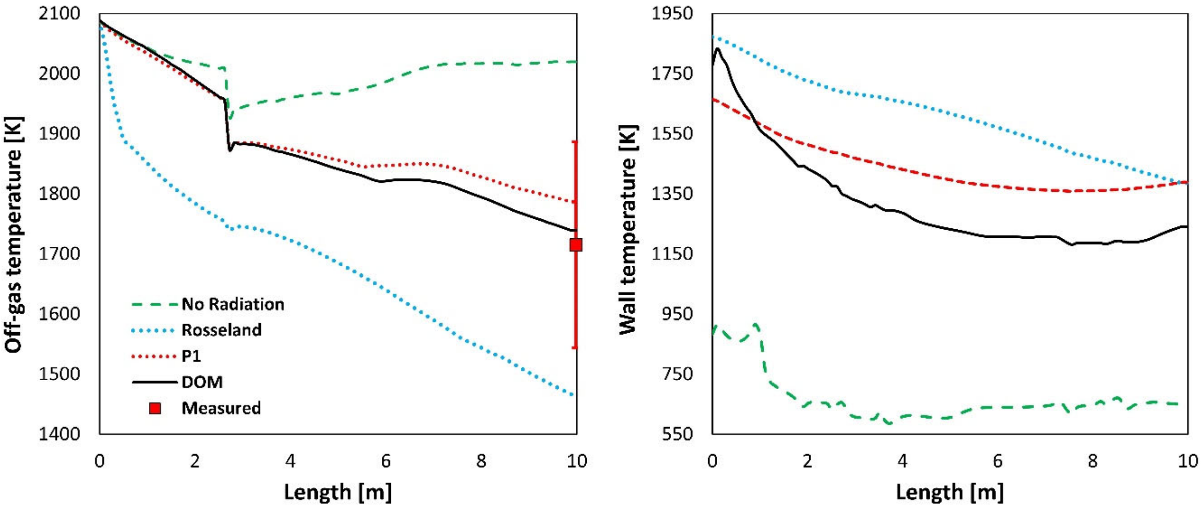

Figure 17. Off-gas and wall temperature profile across the reflux chamber length for different radiation models.

The predicted contour and profiles for Rosseland model is clearly unrealistic and temperature falls rapidly under 1750 K before hitting the oxygen-rich zone. Moreover, the outlet temperature of the reflux camber shows 20% error with respect to the mean measure value and it is even out of the measurement error bars in Figure 17.

The temperature is highly over predicted for the case without radiation model, once again illustrating the importance of the radiation effect.

P1 and DOM have shown quite similar predictions; however, P1 predicts slightly higher temperature around and after oxygen injection zone with a difference of 65 °C compared to DOM model. Nevertheless, both models predict an outlet temperature which is within the measurement error bar.

The wall temperature profile (inner wall in touch with hot flue gas) is also quite similar for P1 and DOM; however, it is predicted higher for Rosseland model. The case without radiation model is in a large discrepancy with other models.

The same conclusion is derived by Habibi et al. [62] who studied the effect of different radiation models on CFD simulation of a steam cracking furnace. They reported unrealistic flame formation for Rosseland and an adiabatic case (without radiation model), but a similar predictions for P1 and DOM.

They have related the lower temperature profile of Rosseland model to its limitation in the prediction of radiation intensity. In Rosseland model, the intensity of radiation is not obtained from a distinct transport equation (as discussed in Section 3) and this leads to an inaccurate temperature profile and flame structure prediction [62].

Figure 18 shows the averaged cross-sectional profile of CO and O_2 and as it can be seen, P1 and DOM predicted quite similar profiles. In all of the cases, the amount of CO is increased before hitting the oxygen injection zone which is related to CO_2 dissociation and carbon gasification at high temperature and in absence of oxygen. The case without radiation model is predicted to have slightly higher CO formation which is related to the higher calculated temperature as depicted in Figure 17. This is due to the fact that higher temperature will lead to a higher CO_2 dissociation into CO.

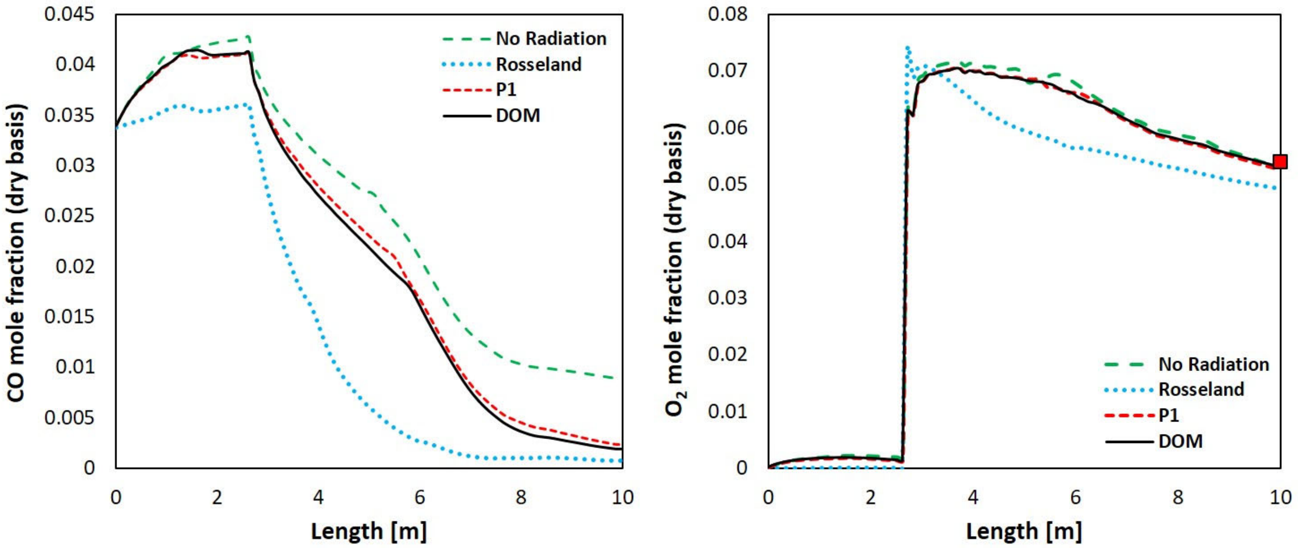

Figure 18. Predicted average cross-sectional CO and O_2 composition profile along the reflux chamber.

On the other hand, since in the case with Rosseland model the temperature falls drastically at the inlet section of the reflux chamber, the predicted dissociation rate of CO_2 will be much lower than the other models and CO profile is nearly constant before hitting the oxygen injection zone. The slight increase in CO amount is related to the carbon particle gasification only. Moreover, for the case with Rosseland radiation model, the amount of CO is always lower than other cases at each cross section and at the outlet of the reflux chamber. This is again due to a lower predicted average temperature across the reflux chamber for Rosseland model which is in favor of CO conversion into CO_2. This effect can also be seen in the oxygen profile which is predicted to be lower at any cross section due to a higher consumption of O_2 (by higher conversion of CO) for Rosseland model.

Figure 19 shows the contour of optical thickness. As depicted, the value of the optical thickness is lower than 1 in all regions for all studied radiation model, illustrating an optically thin medium.

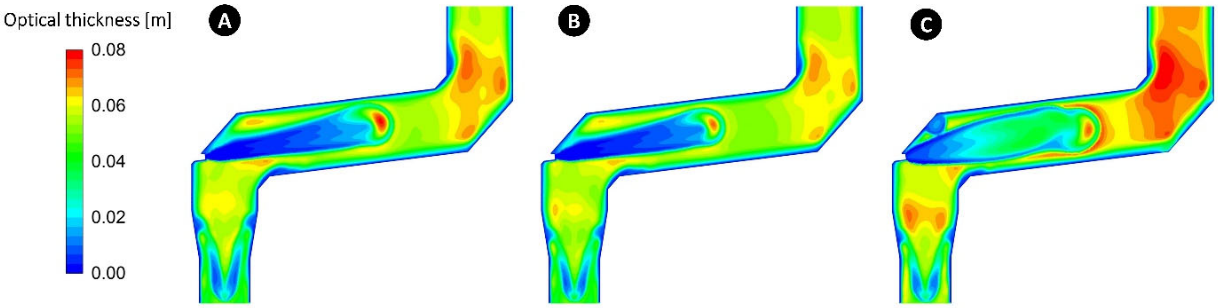

Figure 19. Predicted optical thickness for different radiation model of DOM (**A**), P1 (**B**), and Rosseland (**C**) model.

The predicted opacities are pointing at the fact that Rosseland model should not be used for the current case. All of the models resulted in a very low optical thickness near the combustion zone, but much higher values in the upper parts. Even though P1 model is suitable for cases where optical thickness > 1, but it has predicted values and profiles much closer to DOM which are suitable for all ranges of optical thickness.

Nevertheless, DOM predictions are in better agreement with measured values as shown in Figure 20 for reflux chamber. For the case without radiation model, the heat losses through the reflux chamber walls are predicted much lower than the measured loss due to a very low prediction of the wall temperature (Figure 17). Rosseland model has predicted much higher heat loss due to a lower flue gas temperature and higher wall temperature inside the reflux chamber which increase the driving force for heat transfer to the cold side of the wall (the outer wall in touch with cooling water). The carbon conversion is the highest for the case without radiation model. This is a direct effect of very high temperature prediction that leads to a higher conversion rate of carbon particles. For Rosseland model, even though the temperature along the chamber is the lowest, higher carbon conversion is predicted compared to P1 and DOM. This can be related to a lower predicted CO partial pressure for Rosseland model across the reflux chamber which leads to slightly higher carbon conversion. The predicted carbon conversion using P1 and DOM is close to the measured counterpart.

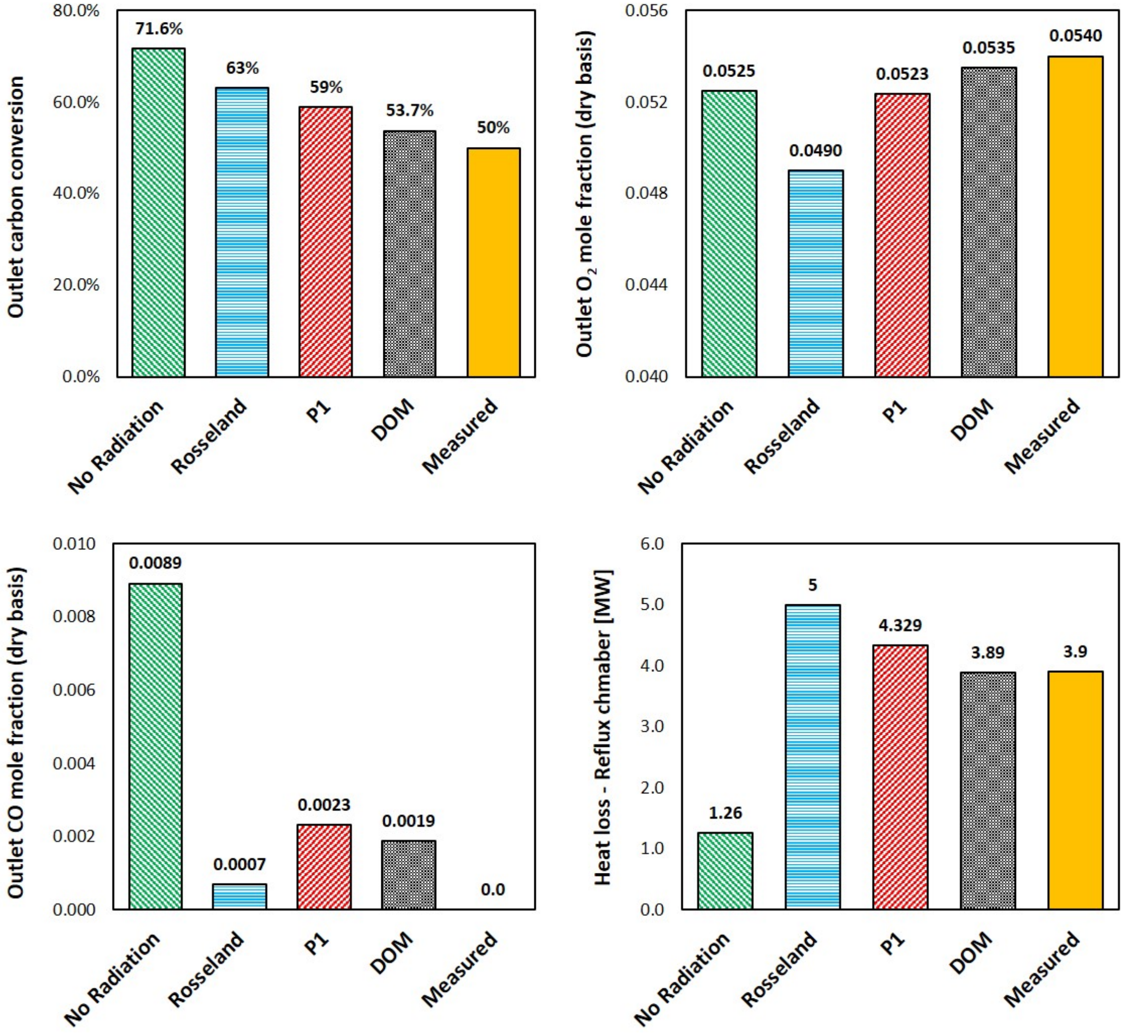

Figure 20. Predicted (different radiation mode) and measured values for different reflux chamber outlet parameters.

The same can be seen for CO outlet mole fraction. Due to a very high predicted temperature profile for the case without radiation model, higher carbon is converted into CO. On the other hand, as mentioned earlier, very high temperature is detrimental for CO conversion and will lead to CO_2 dissociation into CO. Therefore, once the effect of radiation is omitted, higher carbon conversion, low CO conversion, and high CO_2 dissociation will contribute to much higher CO values at the outlet (72% CO conversion). For Rosseland model, lowest outlet CO is predicted due to a much lower predicted temperature profile which is a favorable atmosphere for CO combustion.

Ultimately a quick comparison of simulation time for each radiation model is presented in Figure 21. As illustrated, the including radiation models increase the simulation time by 13%, 11% and 30% for Roseland, P1, and DOM respectively compared to the case without radiation. Comparatively, DOM model requires the longest simulation time while P1 was computationally the cheapest. The same has been reported in numerous studies [62,80]; however the relative increase in simulation time for each model is quite case-dependent.

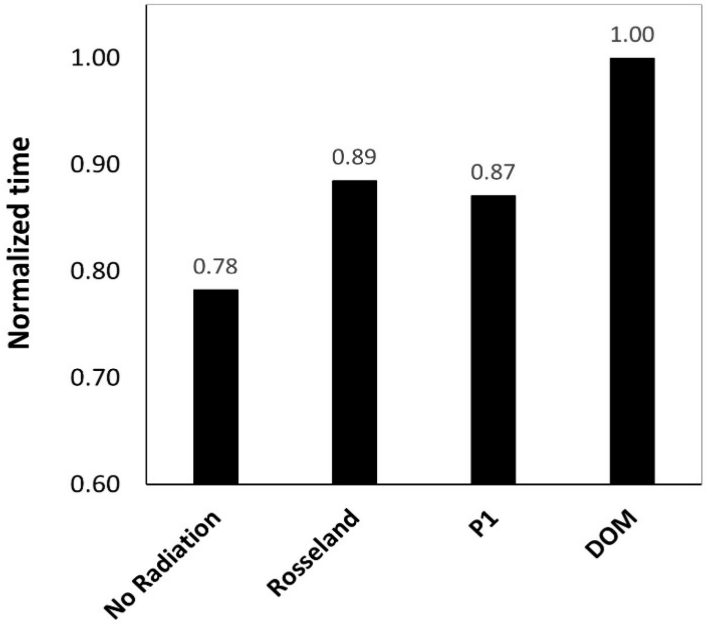

Figure 21. Normalized simulation time for different radiation model.

The following conclusions can be derived from the above analysis for the different radiation models studied:

- For systems with combustion process involved or any system where there is a noticeable difference between fluid and solid surfaces, the radiative heat transfer plays an important and sometimes dominant role. The case without radiation model showed unrealistic and deviated predictions from the measured values.
- The Rosseland model must be used for optically thick mediums (>3) and is not suitable for the current case where computed local optical thickness at any point is lower than 0.1.
- P1 can predict and capture the main feature of the flow and very close to the predicted values by DOM; however, there are still discrepancies between P1 predictions and measured values.
- According to the current results and the references [62,84], P1 model is accurate for optically thick media. It will yield inaccurate results for thinner (more transparent) medium, especially near boundaries, and for anisotropic radiation field. It can also fail in cases with complex geometry, such as congested spaces or geometries with many and large openings.
- P1 model is computationally cheaper and lead to lower calculation times compared to DOM.
- Ultimately, based on the obtained results and the literature review, DOM is generally preferred and seems to be very well-suited for radiation modelling in the current post combustion case.

6. Conclusions

There are many factors that can affect a CFD model performance, reliability, and efficiency. In this study, it was shown that improving only one factor would not necessarily guarantee a proper CFD model with reliable predictions but rather, all sub-models and parameters must be optimized. There may be some rules of thumb for sub-model and parameter selections; however, the model selection is quite case-dependent and sensitivity analysis for a specific case is always required to ensure the reliability of a CFD model.

Form the whole analysis performed in this paper, the following conclusions can be derived:

- For coarse meshes, cell type plays an important role in predictions accuracy but the cell type effect can be ignored for fine meshes.
- Polyhedral mesh grid is always preferred over other types, especially for large-scale and industrial cases with complex geometries and more importantly when computational resources are limited. This is due to the fact that polyhedral mesh exhibits the same accuracy with much lower mesh count thus higher simulation speed.
- Even though k-ω model is more precise for prediction of turbulent nature of the flow, k-ε model is still preferred in industrial and large-scale cases as it requires lower mesh count.
- TCI model selection and kinetic mechanism are important parts of any reactive flow modelling. Based on the literature review and also performed analysis for HIsarna off-gas system, eddy dissipation concept (EDC) model is the most reliable TCI model to predict correct species and temperature profile in a reactive flow.
- Detailed kinetic mechanism is always preferred over global mechanisms for their higher accuracy. However, using detailed mechanisms come at a higher computational cost.
- Including gas–solid reactions could play a vital role in predicting correct temperature and composition profile, specifically for highly exothermic reactions such as carbon oxidation. A sensitivity analysis is needed to include enough number of particles in the calculations that can properly represent the real particle flowrate in the reactive flow.
- For high temperature application, radiation plays an important even a major role. Including radiation model is necessary to take into account the radiation effects especially for internal flow where there is a high temperature difference between the walls and the main flow stream. It becomes even more important for cases where internal reactive flow includes highly exothermic reactions (in the current case, the combustion of CO-H_2 and carbon mixture).
- According to the current results and also the literature reviews, discrete ordinate mode (DOM) is more reliable than the other radiation models (P1 and Rosseland model), which is applicable for all temperature and fluid optical thickness ranges. However, using DOM comes at a higher computational cost relative to the other studied models.
- According to the current case study, it turned out that species composition profile is not as sensitive as temperature profile to sub-model selections, boundary condition, and grid variations. It is suggested to use both temperature profiles and composition profiles for model validation.

Author Contributions: Conceptualization, A.H., E.O. and Y.Y.; data curation, A.H.; formal analysis, A.H.; investigation, J.L.T.H. and K.M.; methodology, A.H., E.O. and Y.Y.; project administration, J.L.T.H., K.M. and Y.Y.; resources, J.L.T.H. and K.M.; software, A.H.; supervision, E.O. and Y.Y.; validation, A.H.; visualization, A.H.; writing—original draft, A.H.; writing—review and editing, A.H., J.L.T.H., K.M. and Y.Y. All authors have read and agreed to the published version of the manuscript.

Funding: This research was funded by EIT RawMaterials grant number [Nr 17209] and The APC was funded by Delft University of Technology.

Institutional Review Board Statement: Not applicable.

Informed Consent Statement: Not applicable.

Data Availability Statement: Some data could be available upon request.

Acknowledgments: The authors would like to thank Sripriya Rajendran for providing input data for CFD simulations.

Conflicts of Interest: The authors declare no conflict of interest.

Nomenclature

Parameter	Description and units
$\boldsymbol{A_r}$	Pre-exponential factor [consistent units]
$\boldsymbol{A_p}$	Particle surface area
$\boldsymbol{a}$	Absorption coefficient
$\boldsymbol{C}$	Constant coefficients
$\boldsymbol{C_{j,r}}$	Molar concentration of species j in reaction r [kmol/m^3]
$\boldsymbol{C_\zeta}$	Volume fraction constant equal to 2.1377
$\boldsymbol{C_\zeta}$	Volume fraction constant
$\boldsymbol{C_\tau}$	Time scale constant equal to 0.4082
$\boldsymbol{D_\omega}$	Cross diffusion term
$\boldsymbol{d_{char}}$	Unreacted core diameter [remaining carbon] [m]
$\boldsymbol{d_p}$	Particle diameter including product [ash] layer [m]
E	Total energy [J/kg]
$\boldsymbol{E_r}$	Activation energy for the reaction [J/kmol]
$\boldsymbol{\vec{F}}$	Force [N]
f_i	Molar fraction of species in the reactions
$\boldsymbol{\vec{g}}$	Gravity constant [m/s^2]
$\boldsymbol{G}$	Incident radiation
$\boldsymbol{G_k}$	Generation of turbulence kinetic energy due to the mean velocity gradients
$\boldsymbol{G_\varepsilon}$	Generation of turbulence dissipation energy
$\boldsymbol{G_b}$	Generation of turbulence kinetic energy due to buoyancy
$\boldsymbol{h_j}$	Enthalpy of species [kJ/kg]
$\boldsymbol{h}$	Heat transfer coefficient [W/m^2-K]
$\boldsymbol{I}$	Spectral radiation intensity
$\boldsymbol{IM}$	Unity matrix
$\boldsymbol{\vec{J_j}\ and\ \vec{J_i}}$	Diffusion flux of species
$\boldsymbol{K_r}$	Equilibrium constant for the r^{th}reaction, computed from
$\boldsymbol{k}$	Turbulent kinetic energy [m^2/s^2],
$\boldsymbol{k_{eff}}$	Effective conductivity [W/m-K]
$\boldsymbol{k_{f,r}}$	Forward rate constant for r^{th} reaction
$\boldsymbol{k_{b,r}}$	Backward rate constant for r^{th} reaction
$\boldsymbol{k_c}$	Mass transfer coefficient [m/s]
$\boldsymbol{k_s}$	Kinetic rate constant [kg/m^2-s-Pa]
$\boldsymbol{k_{diff}}$	Diffusion rate constant [kg/m^2-s-Pa]
$\boldsymbol{k_{dash}}$	Ash diffusion rate constant [kg/m^2-s-Pa]
$\boldsymbol{M_{w,i}}$	Molecular weight of species i [kg/kmol]
$\boldsymbol{m_p}$	Particle mass [kg]
$\boldsymbol{m_p \frac{\vec{u} - \vec{u}_p}{\tau_r}}$	Drag force [N]
$\boldsymbol{\frac{dm_c}{dt}}$	Rate of char depletion [kg/s]
$\boldsymbol{n}$	Spectral index of refraction of the medium
$\boldsymbol{p}$	Pressure [Pa]
$\boldsymbol{P_i - P_i^*}$	Effective pressure [Pa]
$\boldsymbol{q_r}$	Radiative flux [W/m^2]

$\hat{R}_{i,r}$	Arrhenius molar rate of creation/destruction of species i in reaction r [mol/s]
R	Universal gas constant [J/kmol-K]
R_i	Net rate of production/consumption of species by chemical reaction [mol/s]
$R_{char,i}$	Overall rate of solid reaction per unit particle surface area [kg/m^2-s]
S_k and S_ε	User-defined source terms in turbulence equation
S_r	Strain rate magnitude [1/s]
S_i	Source term in species transport
S_h	Source term for the reaction heat and other volumetric heat sources
$\vec{r}$	Position vector [m]
$\vec{s}$	Direction vector
$\vec{s}'$	Scattering direction vector
s	Path length [m]
T_p	Particle temperature [K]
T	Fluid temperature [K]
t	Time [s]
u'	Fluid fluctuating velocity [m/s]
$\bar{u}$	Fluid mean velocity [m/s]
$\vec{u}$	Fluid phase velocity [m/s]
$\vec{u}_p$	Particle velocity [m/s]
Y_M	Contribution of the fluctuating dilatation in compressible turbulence to the overall dissipation rate
Y_k	Dissipation of kinetic energy
Y_ω	Dissipation of eddy dissipation frequency
y_{dis}	Distance to the next surface
Yi	Local mass fraction of each species
Y_i^*	Mass fraction of fine-scale species after reacting over the time τ^*
Y^{eq}	Chemical equilibrium mass fraction
$Y_{i,s}$	Vapor mass fraction at the surface
$Y_{i,\infty}$	Vapor mass fraction in the bulk gas
y_j	Mass fraction of reactive surface species
σ	Stefan-Boltzmann constant
σ_s	Scattering coefficient
Ω'	Solid angle
Γ	Effective diffusivities [kg/m-s]
ε	Energy dissipation rate [m^2/s^3]
μ_t	Turbulent viscosity [m^2/s]
μ	Molecular viscosity [kg/m-s]
ρ	Density of fluid [kg/m^3]
ρ_p	Density of the particle [kg/m^3]
τ_r	Particle relaxation time
τ_{char}	Characteristic time-scale
τ^*	Time scale in EDC
τ_{eff}	Effective shear stress [Pa]
ω	Eddy dissipation frequency [1/s]
σ_k and σ_ω	Turbulent Prandtl numbers
v_i	Corresponding stoichiometric coefficient
$\eta'_{j,r}$	Rate exponent for reactant species j in reaction r

$\boldsymbol{\eta}''_{j,r}$	Rate exponent for reactant species j in reaction r
$\boldsymbol{v}'_{i,r}$	Stoichiometric coefficient for reactant i in reaction r
$\boldsymbol{v}''_{i,r}$	Stoichiometric coefficient for product i in reaction r
$\boldsymbol{\theta}$	Net effect of third bodies on the reaction rate
$\boldsymbol{\gamma}_{j,r}$	Third-body efficiency of the j^{th} species in the r^{th} reaction
$\boldsymbol{\beta}_r$	Temperature exponent
$\boldsymbol{\zeta}^*$	Length fraction of the fine scales
$\boldsymbol{\partial}$	Porosity of the ash layer
$\boldsymbol{\vartheta}$	kinematic viscosity [m^2/s]

Appendix A. List of Literature Review for Sub-Model Sections

Table A1. Summary of utilized mechanisms for different reactive flow modelling

Fuel Mixture	Oxidizer	Pressure [atm]	Mechanism	Number of Species	Number of Reactions	Reference
CO-H_2O	Air	1–20 atm	Detailed	13	28	[37]
CO-H_2-H_2O	Air	1	Detailed	8	31	[85]
CO/H_2/CH_4	Air	1	Detailed GRI	53	325	[86]
CO/H_2	Air/O_2	1	Detailed	14	30	[38]
CO/H_2	Air	40–200	Detailed	12	27	[87]
CO/H_2		1–20	Detailed	14	30	[39]
CH_4/CO/H_2	Air	1	Detailed GRI	53	325	[88]
CH_4/CO/H_2	Air	1	Detailed GRI	53	325	[89]
CH_4/CO/H_2	Air	1	Detailed USC II	111	784	[89]
CO/H_2	Air	1–5	Detailed GRI and mechanism from [38]	53	325	[24]
CO/H_2	Air/O_2	1–10	Detailed	14	33	[40]
CH_4/CO/H_2		1–40	Detailed GRI Reduced GRI NUIG [41] Heghes [90] Frenklach [42,91]			[43–45]
CO/H_2	Air/O_2	1	Detailed	14	33	[47,48]
CH_4/CO	Air	1	Global 3 step Westbrook-Dryer	5	3	[50]
CH_4/CO/H_2	Air	1	Global 4 step Jones-Lindstedt	6	4	[50]
CH_4/CO/H_2	Air	1	Global 6 step modified Jones-Lindstedt	9	6	[50]
CO/H_2	Air/O_2	1–20	Global 5 step	8	5	[25]

Table A2. Summary of utilized TCI models for different reactive flow modelling at different scales

Application	Scale	Fuel Mixture	Mechanism	TCI Model	Reference
Hydrogen jet	Experimental	H_2	Detailed (16 and 37 reactions)	EDM/EDC	[92]
Gas burner	Pilot	C_2H_6/CH_4/CO/H_2	Reduced GRI	EDC	[93]
Gas burner	Experimental	CH_4/CO/H_2	GRI	EDC	[94–96]
Wood pellet burner	Domestic	Solid biomass CO-H_2	Global	EDC	[97]

Sulfur recovery unit (SRU)	Industrial	H_2S/CH_4	Detailed (432 reactions)	EDC	[98]
Gas burner	Pilot	CH_4/H_2	GRI DRM-22 [99]	EDC	[100,101]
Gas burner	Industrial	CH_4/H_2	Global DRM-19 [99] GRI	EDC/FR-EDM	[58]
Entrained Flow Coal Gasifier	Experimental/ pilot	Coal /CO/H_2	Global [14,22,102] GRI CRECK [103]	EDC/FR-EDM	[51]
Cyclonic gas burner	Experimental	C_3H_8	San Diego [104]	EDC	[105]
JHC burner	Experimental	ethylene/H_2	GRI POLIMI [106]	EDC	[107]
Gas burner	Experimental	CH_4	GRI DRM 19 global	EDC	[14]
Burner	Experimental	CH_4/CO	SFM KEE	EDC	[108]
burner	Pilot	H_2		EDM	[109]
pulsejet engine	Experimental	$C_{12}H_{23}/CH_4$		EDM	[110]
Furnace	Experimental	CH_4/CO/H_2	DRM19	EDC	[111]
rocket combustion chamber	Experimental	CH_4/CO/H_2	detailed (18 reactions) [112]	EDC	[113]
Coal burner	Experimental	pulverized coal/CO/H_2	Detailed frank	EDM/EDC	[56]
furnace	Industrial	Natural gas	Global 4 step	EDM	[114]
Entrained flow gasifier	Pilot	Coal/CO/H_2	Reduced GRI	EDC	[115]
Entrained bed gasifier	Pilot	Coal/CO/H_2	Detailed	FR-EDM	[116]
high-velocity oxy-fuel	Experimental	H_2	Global 2 step	EDM/EDC	[53]
Thermal cracking	Pilot	$C_2H_6/C_3H_8/C_4H_{10}$	Detailed (23 reactions)	FR-EDM	[117]
Thermal cracking	Pilot	C_3H_8	Detailed (23 reactions) [118]	EDC	[119]
Micro mixing	Experimental	*Boric acid*	Global 3 step	FR-EDM	[120]
Solid Fuel Ramjet	Experimental	C_2H_4	Global 3 step	EDM/FR-EDM	[52]
ethylene cracking furnaces	Pilot		Detailed (22 reactions)	FR-EDM	[121]
Steam methane reforming furnace	Industrial	CH_4	Global (3 step)	FR-EDM	[82]

Table A3. Summary of utilized radiation modelling for different high temperature reactive flow applications

Application	**Scale**	**Temperature Range [K]**	**Fuel**	**Radiation Model**	**Reference**
Steam methane reforming furnace	Pilot	1100–1400	CH_4	DOM	[122]
Ethylene cracking furnaces	Pilot	300–2100	n-Paraffins/i-Paraffins/Olefins	DOM	[121]
Post combustion chamber	Pilot	300–2000	CO/H_2	P1	[79]
Methane combustor	pilot	300–2325	CH_4/H_2	P1	[123]

Ethylene furnace	Industrial	300–2150	CH_4/H_2—complex feed	DOM	[124]
Sulphur removal unit	Industrial	-	H_2S	DOM	[98]
hydrogen production reformer	Industrial	650–2500	CH_4	P1	[81]
naphtha thermal cracking furnaces	Industrial	300–1550	$CH_4/C_2H_4/C_2H_6/C_3H_8/H_2$	DOM	[17]
semi-suspension biomass fired industrial	Industrial	300–1600	Bagasse	DOM	[125]
Steam methane reforming furnace	Industrial	500–2000	CH_4	DOM	[82]
Mild combustor	Industrial	300–2519	CH_4/H_2	DOM	[58]
Gas burner	Industrial	-	$C_2H_6/CH_4/CO/H_2$	DOM	[114]
entrained-flow gasifier	Industrial	300–2250	Coal/CO/H_2	P1	[115]
Gasifier	Industrial	600–1100	Wood chips	DOM	[126]

References

1. Tillman, D.A.; Duong, D.N.B.; Harding, N.S. *Chapter 7—Modeling and Fuel Blending*; Butterworth-Heinemann: Boston, MA, USA, 2012; pp. 271–293.
2. Vásquez, E.; Eldredge, T. Process modeling for hydrocarbon fuel conversion: Science and Technology. In *Advances in Clean Hydrocarbon Fuel Processing*; Elsevier: Amsterdam, The Netherlands, 2011; pp. 509–545. Available online: https://www.sciencedirect.com/science/article/pii/B9781845697273500184 (accessed on 1 November 2021).
3. Uriz, I.; Arzamendi, G.; Diéguez, P.M.; Gandía, L.M. Chapter 17—Computational Fluid Dynamics as a Tool for Designing Hydrogen Energy Technologies. In *Renewable Hydrogen Technologies Production, Purification, Storage, Applications and Safety*; Elsevier: Amsterdam, The Netherlands, 2013; pp. 401–435.
4. Moser, A.; Schäulin, A.; Davidson, L.; Corrado, V.; Dorer, V.; Koschenz, M.; Schälin, A. Design with Modeling Techniques. In *Industrial Ventilation Design Guidebook*; Academic Press: Cambridge, MA, USA, 2001; pp. 1025–1104. https://doi.org/10.1016/b978-012289676-7/50014-x.
5. Juretić, F.; Gosman, A.D. Error Analysis of the Finite-Volume Method with Respect to Mesh Type. *Numer. Heat Transf. Part B Fundam.* **2010**, *57*, 414–439, https://doi.org/10.1080/10407791003685155.
6. Duan, R.; Liu, W.; Xu, L.; Huang, Y.; Shen, X.; Lin, C.-H.; Liu, J.; Chen, Q.; Sasanapuri, B. Mesh Type and Number for the CFD Simulations of Air Distribution in an Aircraft Cabin. *Numer. Heat Transfer Part B Fundam.* **2015**, *67*, 489–506. https://doi.org/10.1080/10407790.2014.985991.
7. Xie, B.; Xiao, F. A multi-moment constrained finite volume method on arbitrary unstructured grids for incompressible flows. *J. Comput. Phys.* **2016**, *327*, 747–778.
8. Xie, B.; Deng, X.; Liao, S. High-fidelity solver on polyhedral unstructured grids for low-Mach number compressible viscous flow. *Comput. Methods Appl. Mech. Eng.* **2019**, *357*, 112584.
9. Yu, G.; Yu, B.; Sun, S.; Tao, W.-Q. Comparative Study on Triangular and Quadrilateral Meshes by a Finite-Volume Method with a Central Difference Scheme. *Numer. Heat Transfer Part B Fundam.* **2012**, *62*, 243–263. https://doi.org/10.1080/10407790.2012.709416.
10. MSosnowski; Krzywanski, J.; Gnatowska, R. Polyhedral meshing as an innovative approach to computational domain discretization of a cyclone in a fluidized bed CLC unit. *E3S Web Conf.* **2017**, *14*, 01027. https://doi.org/10.1051/e3sconf/20171401027.
11. Tu, J.; Yeoh, G.H.; Liu, C. Chapter 6—Practical Guidelines for CFD Simulation and Analysis. In *Computational Fluid Dynamics-A Practical Approach*, 2nd ed.; Butterworth-Heinemann*:* Amsterdam, The Netherlands, 2013; p. 219–273.
12. Sosnowski, M.; Gnatowska, R.; Grabowska, K.; Krzywański, J.; Jamrozik, A. Numerical Analysis of Flow in Building Arrangement: Computational Domain Discretization. *Appl. Sci.* **2019**, *9*, 941. https://doi.org/10.3390/app9050941.
13. Zhang, H.; Tang, S.; Yue, H.; Wu, K.; Zhu, Y.; Liu, C.; Liang, B.; Li, C. Comparison of Computational Fluid Dynamic Simulation of a Stirred Tank with Polyhedral and Tetrahedral Meshes. *Iran. J. Chem. Chem. Eng.* **2020**, *39*, 311–319.
14. Westbrook, C.K.; Dryer, F.L. Simplified Reaction Mechanisms for the Oxidation of Hydrocarbon Fuels in Flames. *Combust. Sci. Technol.* **1981**, *27*, 31–43. https://doi.org/10.1080/00102208108946970.
15. Westbrook, C.K.; Dryer, F.L. Chemical kinetics and modeling of combustion processes. *Symp. Int. Combust.* **1981**, *18*, 749–767. https://doi.org/10.1016/s0082-0784(81)80079-3.
16. Mulder, M. O2/CH4 Kinetic Mechanisms for Aerospace Applications at Low Pressure and Temperature, Validity Ranges and Comparison. In *Aeronautics and Astronautics*; IntechOpen: London, UK, 2011; p. 13.
17. Rezaeimanesh, M.; Ghoreyshi, A.A.; Peyghambarzadeh, S.; Hashemabadi, S.H. A coupled CFD simulation approach for investigating the pyrolysis process in industrial naphtha thermal cracking furnaces. *Chin. J. Chem. Eng.* **2021**, *44*, 528–542. https://doi.org/10.1016/j.cjche.2021.03.028.

18. Castilla, G.M.; Montañés, R.M.; Pallarès, D.; Johnsson, F. Comparison of the Transient Behaviors of Bubbling and Circulating Fluidized Bed Combustors. *Heat Transf. Eng.* **2022**, *44*, 303–316.
19. Chen, L.; Ghoniem, A.F. Modeling CO2 Chemical Effects on CO Formation in Oxy-Fuel Diffusion Flames Using Detailed, Quasi-Global, and Global Reaction Mechanisms. *Combust. Sci. Technol.* **2014**, *186*, 829–848.
20. Andersen, J.; Rasmussen, C.L.; Giselsson, T.; Glarborg, P. Global Combustion Mechanisms for Use in CFD Modeling under Oxy-Fuel Conditions. *Energy Fuels* **2009**, *23*, 1379–1389. https://doi.org/10.1021/ef8003619.
21. Novosselov, I.V.; Malte, P.C. Development and Application of an Eight-Step Global Mechanism for CFD and CRN Simulations of Lean-Premixed Combustors. In Proceedings of the ASME Turbo Expo 2007: Power for Land, Sea, and Air, Montreal, QC, Canada, 14–17 May 2007; pp. 769–779.
22. Jones, W.; Lindstedt, R. Global reaction schemes for hydrocarbon combustion. *Combust. Flame* **1988**, *73*, 233–249. https://doi.org/10.1016/0010-2180(88)90021-1.
23. GRI-Mech. GRI 3.0 Mechanism. Available online: http://combustion.berkeley.edu/gri-mech/overview.html (accessed on 8 April 2022)
24. Natarajan; Lieuwen, T.; Seitzman, J. Laminar flame speeds of H2/CO mixtures: Effect of CO2 dilution, preheat temperature, and pressure. *Combust. Flame* **2007**, *151*, 104–119. https://doi.org/10.1016/j.combustflame.2007.05.003.
25. Nikolaou, Z.M.; Chen, J.Y.; Swaminathan, N. A 5-step reduced mechanism for combustion of CO/H2/H2O/CH4/CO2 mixtures with low hydrogen/methane and high H2O content. *Combust Flame* **2013**, *160*, 56–75.
26. Iavarone, S.; Parente, A. NOx Formation in MILD Combustion: Potential and Limitations of Existing Approaches in CFD. *Front. Mech. Eng.* **2020**, *6*, 13
27. Dally, B.; Karpetis, A.; Barlow, R. Structure of turbulent non-premixed jet flames in a diluted hot coflow. *Proc. Combust. Inst.* **2002**, *29*, 1147–1154. https://doi.org/10.1016/s1540-7489(02)80145-6.
28. Sung, C.; Law, C.; Chen, J.-Y. Augmented reduced mechanisms for NO emission in methane oxidation. *Combust. Flame* **2001**, *125*, 906–919. https://doi.org/10.1016/s0010-2180(00)00248-0.
29. Xu, H.; Liu, F.; Wang, Z.; Ren, X.; Chen, J.; Li, Q.; Zhu, Z. A Detailed Numerical Study of NOx Kinetics in Counterflow Methane Diffusion Flames: Effects of Fuel-Side versus Oxidizer-Side Dilution. *J. Combust.* **2021**, *2021*, 6642734. https://doi.org/10.1155/2021/6642734.
30. Weydahl, T.; Ertesvåg, I.; Gran, I.; Magnussen, B.; Kilpinen, P. Prediction of Nitrogen Oxide Formation in Ammonia-Doped Turbulent Syngas Jet Flames. In Proceedings of the 29th International Symposium on Combustion, Sapporo, Japan, 21–26 July 2022.
31. Zahirović, S.; Scharler, R.; Kilpinen, P.; Obernberger, I. Validation of flow simulation and gas combustion sub-models for the CFD-based prediction of NOx formation in biomass grate furnaces. *Combust. Theory Model.* **2010**, *15*, 61–87.
32. Hu, X.Z.; Yu, Q.B.; Li, Y.M. Skeletal and Reduced Mechanisms of Methane at O2/CO2 Atmosphere. *Chem. J. Chin. Univ.* **2018**, *39*, 95–101.
33. Wang, W. Studies on the Efficient Reduction Methods for the Combustion Chemical Kinetic Mechanism of Fuel. Ph.D. Thesis, Chongqing University, Chongqing, China, 2016.
34. Gou, X.L.; Wang, W.; Gui, Y. Methane Reaction Mechanism Reduction Using Paths Flux Analysis of Three Generations Method. *J. Eng. Thermophys.* **2014**, *35*, 1870–1873.
35. Liu, H.; Chen, F.; LIU, H.; Zheng, Z.H.; Yang, S.H. 18-step reduced mechanism for methane/air premixed supersonic combustion. *J. Combust. Sci. Technol.* **2012**, *18*, 467–472.
36. Lu, H.; Liu, F.; Wang, Y.; Fan, X.; Yang, J.; Liu, C.; Xu, G. Mechanism Reduction and Bunsen Burner Flame Verification of Methane. *Energies* **2018**, *12*, 97. https://doi.org/10.3390/en12010097.
37. Kim, T.J.; Yetter, R.A.; Dryer, F.L. New results on moist CO oxidation: high pressure, high temperature experiments and comprehensive kinetic modeling. *Symp. Int. Combust.* **1994**, *25*, 759–766. https://doi.org/10.1016/s0082-0784(06)80708-3.
38. Davis, S.G.; Joshi, A.V.; Wang, H.; Egolfopoulos, F. An optimized kinetic model of H2/CO combustion. *Proc. Combust. Inst.* **2005**, *30*, 1283–92.
39. Saxena, P.; Williams, F.A. Testing a small detailed chemical-kinetic mechanism for the combustion of hydrogen and carbon monoxide. *Combust Flame* **2006**, *145*, 316–323.
40. Sun, H.; Yang, S.; Jomaas, G.; Law, C. High-pressure laminar flame speeds and kinetic modeling of carbon monoxide/hydrogen combustion. *Proc. Combust. Inst.* **2007**, *31*, 439–446. https://doi.org/10.1016/j.proci.2006.07.193.
41. Healy, D.; Donato, N.; Aul, C.; Petersen, E.; Zinner, C.; Bourque, G.; Curran, H. Isobutane ignition delay time measurements at high pressure and detailed chemical kinetic simulations. *Combust. Flame* **2010**, *157*, 1540–1551. https://doi.org/10.1016/j.combustflame.2010.01.011.
42. Frenklach, M. Reaction mechanism of soot formation in flames. *Phys. Chem. Chem. Phys.* **2002**, *4*, 2028–2037. https://doi.org/10.1039/b110045a.
43. Fischer, M.; Jiang, X. An investigation of the chemical kinetics of biogas combustion. *Fuel* **2015**, *150*, 711–720.
44. Fischer, M.; Jiang, X. An assessment of chemical kinetics for bio-syngas combustion. *Fuel* **2014**, *137*, 293–305.
45. Fischer, M.; Jiang, X. A chemical kinetic modelling study of the combustion of CH4–CO–H2–CO2 fuel mixtures. *Combust Flame* **2016**, *167*, 274–293.
46. Maas, U.; Warnatz, J. Ignition processes in carbon-monoxide-hydrogen-oxygen mixtures. *Symp. Int. Combust.* **1989**, *22*, 1695–704.

47. Frassoldati, A.; Faravelli, T.; Ranzi, E. The ignition, combustion and flame structure of carbon monoxide/hydrogen mixtures. Note 1: Detailed kinetic modeling of syngas combustion also in presence of nitrogen compounds. *Int. J. Hydrog. Energy* **2007**, *32*, 3471–3485. https://doi.org/10.1016/j.ijhydene.2007.01.011.
48. Cuoci, A.; Frassoldati, A.; Buzzi Ferraris, G.; Faravelli, T.; Ranzi, E. The ignition, combustion and flame structure of carbon monoxide/hydrogen mixtures. Note 2: Fluid dynamics and kinetic aspects of syngas combustion. *Int. J. Hydrog. Energy* **2007**, *32*, 3486–500.
49. Graça, M.; Duarte, A.; Coelho, P.; Costa, M. Numerical simulation of a reversed flow small-scale combustor. *Fuel Process. Technol.* **2012**, *107*, 126–137. https://doi.org/10.1016/j.fuproc.2012.06.028.
50. Frassoldati, A.; Cuoci, A.; Faravelli, T.; Ranzi, E.; Candusso, C.; Tolazzi, D. Simplified kinetic schemes for oxy-fuel combustion. In Proceedings of the 1st International Conference on Sustainable Fossil Fuels for Future Energy, 2009. Available online: https://www.researchgate.net/profile/Eliseo-Ranzi/publication/237494009_Simplified_kinetic_schemes_for_oxy-fuel_combustion/links/546f61b50cf24af340c08922/Simplified-kinetic-schemes-for-oxy-fuel-combustion.pdf (accessed on 1 November 2021).
51. Mularski, J.; Modliński, N. Impact of Chemistry–Turbulence Interaction Modeling Approach on the CFD Simulations of Entrained Flow Coal Gasification. *Energies* **2020**, *13*, 6467.
52. Musa, O.; Xiong, C.; Changsheng, Z.; Min, Z. Combustion modeling of unsteady reacting swirling flow in solid fuel ramjet. In Proceedingds of the 2017 International Conference on Mechanical, System and Control Engineering (ICMSC), St. Petersburg, Russia, 19–21 May 2017; pp. 115–120. https://doi.org/10.1109/icmsc.2017.7959454.
53. Emami, S.; Jafari, H.; Mahmoudi, Y. Effects of Combustion Model and Chemical Kinetics in Numerical Modeling of Hydrogen-Fueled Dual-Stage HVOF System. *J. Therm. Spray Technol.* **2019**, *28*, 333–345. https://doi.org/10.1007/s11666-019-00826-8.
54. May, S.; Karl, S.; Bo, O. Development of an Eddy Dissipation Model for the use in Numerical Hybrid Rocket Engine Combustion Simulation. In Proceedings of the 7th European Conference for Aeronautics and Space Sciences (EUCASS), Milan, Italy, 3–6 July 2017.
55. Elwina; Yunardi; Bindar, Y.; Syukran. Simulation of the Influence of Air Preheat Combustion on the Temperature of Propane Turbulent Flame Using Probability Density Function Approach and Eddy Dissipation Model. *Adv. Mat. Res.* **2014**, *871*, 95–100.
56. Vascellari, M.; Cau, G. Influence of turbulence–chemical interaction on CFD pulverized coal MILD combustion modeling. *Fuel* **2012**, *101*, 90–101.
57. Rohani, B.; Wahid, M.A.; Sies, M.M.; Saqr, K.M. Comparison of eddy dissipation model and presumed probability density function model for temperature prediction in a non-premixed turbulent methane flame. In *Proceedings of the 4th International Meeting of Advances in Thermofluids (IMAT 2011)*; AIP Conference Proceedings: Perlis, Malaysia, 2012; Volume 1440, pp. 384–391. https://doi.org/10.1063/1.4704240.
58. Parente, A.; Galletti, C.; Tognotti, L. Effect of the combustion model and kinetic mechanism on the MILD combustion in an industrial burner fed with hydrogen enriched fuels. *Int. J. Hydrog. Energy* **2008**, *33*, 7553–7564. https://doi.org/10.1016/j.ijhydene.2008.09.058.
59. Olivieri, A.; Vegliò, F. Process simulation of natural gas steam reforming: Fuel distribution optimisation in the furnace. *Fuel Process. Technol.* **2008**, *89*, 622–632.
60. Liesche, G.; Sundmacher, K. Radiation-based model reduction for the optimization of high temperature tube bundle reactors: Synthesis of hydrogen cyanide. *Comput. Chem. Eng.* **2019**, *127*, 186–199.
61. Yu, Z.; Cao, E.; Wang, Y.; Zhou, Z.; Dai, Z. Simulation of natural gas steam reforming furnace. *Fuel Process. Technol.* **2006**, *87*, 695–704. https://doi.org/10.1016/j.fuproc.2005.11.008.
62. Habibi, A.; Merci, B.; Heynderickx, G. Impact of radiation models in CFD simulations of steam cracking furnaces. *Comput. Chem. Eng.* **2007**, *31*, 1389–1406. https://doi.org/10.1016/j.compchemeng.2006.11.009.
63. Modest, M.F. The Weighted-Sum-of-Gray-Gases Model for Arbitrary Solution Methods in Radiative Transfer. *J. Heat Transf.* **1991**, *113*, 650–656. https://doi.org/10.1115/1.2910614.
64. Krishnamoorthy, G. A new weighted-sum-of-gray-gases model for CO2–H2O gas mixtures. *Int. Commun. Heat Mass Transf.* **2010**, *37*, 1182–1186. https://doi.org/10.1016/j.icheatmasstransfer.2010.07.007.
65. Cassol, F.; Brittes, R.; França, F.H.; Ezekoye, O.A. Application of the weighted-sum-of-gray-gases model for media composed of arbitrary concentrations of H 2 O, CO 2 and soot. *Int. J. Heat Mass Transf.* **2014**, *79*, 796–806. https://doi.org/10.1016/j.ijheatmasstransfer.2014.08.032.
66. Kim, O.J.; Song, T.-H. Implementation of the weighted sum of gray gases model to a narrow band: Application and validity. *Numer. Heat Transfer Part B Fundam.* **1996**, *30*, 453–468. https://doi.org/10.1080/10407799608915093.
67. Levenspiel, O. *Chemical Reaction Engineering*; Wiley: New York, NY, USA, 1972; Volume 2.
68. Stapountzis, H.; Tzavellas, P.; Moros, T. Effects of Turbulence on the Mixing and Chemical Reaction for Cross Flow and Coflowing jets BT. In *Advances in Turbulence 3*; Johansson, A.V., Alfredsson, P.H., Eds.; Springer: Berlin/Heidelberg, Germany, 1991; pp. 300–311.
69. Glassman, I.; Eberstein, I.J. Turbulence effects in chemical reaction kinetics measurements. *AIAA J.* **1963**, *1*, 1424–1426.
70. Magnussen, B.; Hjertager, B. On mathematical modeling of turbulent combustion with special emphasis on soot formation and combustion. *Symp. Int. Combust.* **1977**, *16*, 719–729. https://doi.org/10.1016/s0082-0784(77)80366-4.
71. Poinsot, T.; Veynante, D. *Theoretical and Numerical Combustion*; RT Edwards Inc.: Spring Hope, NC, USA, 2005.

72. Rebola, P.; Coelho, J.; Costa, M. Assessment of the Performance of Several Turbulence and Combustion Models in the Numerical Simulation of a Flameless Combustor. *Combust. Sci. Technol.* **2013**, *185*, 600–626. https://doi.org/10.1080/00102202.2012.739222.
73. Toporov, D.D. Chapter 4—Mathematical Modelling and Model Validations. In *Combustion of Pulverised Coal in a Mixture of Oxygen and Recycled Flue Gas*; Elsevier: Boston, MA, USA, 2014; pp. 51–97.
74. Morsi, S.A.; Alexander, A.J. An investigation of particle trajectories in two-phase flow systems. *J. Fluid Mech.* **1972**, *55*, 193–208. https://doi.org/10.1017/s0022112072001806.
75. Mofakham, A.A.; Ahmadi, G. Improved Discrete Random Walk Stochastic Model for Simulating Particle Dispersion and Deposition in Inhomogeneous Turbulent Flows. *J. Fluids Eng.* **2020**, *142*, 101401. https://doi.org/10.1115/1.4047538.
76. Hosseini, A.; Dhiman, V.; Meijer, K.; Zeilstra, C.; Hage, J.; Peeters, T.; Offerman, E.; Yang, Y. CFD modelling of the off-gas system HIsarna iron making process part 2: reflux chamber geometry modification and effects on flow behaviour. *Ironmak. Steelmak.* **2022**, *49*, 783–794. https://doi.org/10.1080/03019233.2022.2060457.
77. Wen, C.Y.; Chaung, T.Z. Entrainment Coal Gasification Modeling. *Ind. Eng. Chem. Process Des. Dev.* **1979**, *18*, 684–695.
78. Wang, W.; Cao, Y.; Okaze, T. Comparison of hexahedral, tetrahedral and polyhedral cells for reproducing the wind field around an isolated building by LES. *Build. Environ.* **2021**, *195*, 107717.
79. Sripriya, R.; Peeters, T.; Meijer, K.; Zeilstra, C.; Van Der Plas, D. Computational fluid dynamics and combustion modelling of HIsarna incinerator. *Ironmak. Steelmak.* **2016**, *43*, 192–202. https://doi.org/10.1179/1743281215y.0000000031.
80. Labiscsak, L.; Straffelini, G.; Corbetta, C.; Bodino, M. Fluid dynamics of a post-combustion chamber in electric arc steelmaking plants. *Comput. Methods Exp. Meas.* **2011**, *51*, 205–214, https://doi.org/10.2495/cmem110191.
81. Chen, P.; Du, W.; Zhang, M.; Duan, F.; Zhang, L. Numerical studies on heat coupling and configuration optimization in an industrial hydrogen production reformer. *Int. J. Hydrog. Energy* **2018**, *44*, 15704–15720. https://doi.org/10.1016/j.ijhydene.2018.10.238.
82. Tran, A.; Aguirre, A.; Durand, H.; Crose, M.; Christofides, P.D. CFD modeling of a industrial-scale steam methane reforming furnace. *Chem. Eng. Sci.* **2017**, *171*, 576–598. https://doi.org/10.1016/j.ces.2017.06.001.
83. ANSYS Inc. *Guide AFU*; ANSYS Inc.: Canonsburg, PA, USA, 2013.
84. Keramida, E.; Liakos, H.; Founti, M.; Boudouvis, A.; Markatos, N. Radiative heat transfer in natural gas-fired furnaces. *Int. J. Heat Mass Transf.* **2000**, *43*, 1801–1809. https://doi.org/10.1016/s0017-9310(99)00244-6.
85. Wang, W.; Rogg, B. Reduced kinetic mechanisms and their numerical treatment I: Wet CO flames. *Combust. Flame* **1993**, *94*, 271–292.
86. Vagelopoulos, C.; Egolfopoulos, F. Laminar flame speeds and extinction strain rates of mixtures of carbon monoxide with hydrogen, methane, and air. *Symp. Int. Combust.* **1994**, *25*, 1317–1323. https://doi.org/10.1016/s0082-0784(06)80773-3.
87. Li, W.; Zou, C.; Yao, H.; Lin, Q.; Fu, R.; Luo, J. An optimized kinetic model for H2/CO combustion in CO2 diluent at elevated pressures. *Combust Flame* **2022**, *241*, 112093.
88. Singh, D.; Nishiie, T.; Tanvir, S.; Qiao, L. An experimental and kinetic study of syngas/air combustion at elevated temperatures and the effect of water addition. *Fuel* **2012**, *94*, 448–456. https://doi.org/10.1016/j.fuel.2011.11.058.
89. He, Y.; Wang, Z.; Yang, L.; Whiddon, R.; Li, Z.; Zhou, J.; Cen, K. Investigation of laminar flame speeds of typical syngas using laser based Bunsen method and kinetic simulation. *Fuel* **2012**, *95*, 206–213, https://doi.org/10.1016/j.fuel.2011.09.056.
90. Heghes, C. Soot Formation Modeling During Hydrocarbon Pyrolysis and Oxidation Behind Shock Waves. Ph.D. Thesis, University of Heidelberg, Heidelberg, Germany, 2006.
91. Wang, H.; Frenklach, M. A detailed kinetic modeling study of aromatics formation in laminar premixed acetylene and ethylene flames. *Combust Flam* **1997**, *110*, 173–221.
92. Vankova, O.S. *Comparison of Turbulence/Chemistry Interaction Models in the Problem of Ignition a Parallel Hydrogen Jet in a Supersonic Air Flow*; AIP Conference Proceedings: Perlis, Malaysia, 2021; Volume 2351. https://doi.org/10.1063/5.0053925.
93. Lewandowski, M.T.; Pozorski, J. Assessment of turbulence-chemistry interaction models in the computation of turbulent nonpremixed flames. *J. Phys. Conf. Ser.* **2016**, *760*, 012015. https://doi.org/10.1088/1742-6596/760/1/012015.
94. Christo, F.; Dally, B. Modeling turbulent reacting jets issuing into a hot and diluted coflow. *Combust. Flame* **2005**, *142*, 117–129. https://doi.org/10.1016/j.combustflame.2005.03.002.
95. De, A.; Oldenhof, E.; Sathiah, P.; Roekaerts, D. Numerical Simulation of Delft-Jet-in-Hot-Coflow (DJHC) Flames Using the Eddy Dissipation Concept Model for Turbulence–Chemistry Interaction. *Flow Turbul. Combust.* **2011**, *87*, 537–567. https://doi.org/10.1007/s10494-011-9337-0.
96. De, A.; Dongre, A. Assessment of Turbulence-Chemistry Interaction Models in MILD Combustion Regime. *Flow Turbul. Combust.* **2015**, *94*, 439–478.
97. Chapela, S.; Porteiro, J.; Costa, M. Effect of the Turbulence–Chemistry Interaction in Packed-Bed Biomass Combustion. *Energy Fuels* **2017**, *31*, 9967–9982. https://doi.org/10.1021/acs.energyfuels.7b00516.
98. Mahmoodi, B.; Hosseini, S.H.; Ahmadi, G.; Raj, A. CFD simulation of reactor furnace of sulfur recovery units by considering kinetics of acid gas (H_2S and CO_2) destruction. *Appl. Therm. Eng.* **2017**, *123*, 699–710. https://doi.org/10.1016/j.applthermaleng.2017.05.148.
99. DRM Mechanism. Available online: http://combustion.berkeley.edu/drm/ (accessed on 1 November 2021).
100. Mardani, A. Optimization of the Eddy Dissipation Concept (EDC) model for turbulence-chemistry interactions under hot diluted combustion of CH4/H2. *Fuel* **2017**, *191*, 114–219.

101. Mardani, A.; Tabejamaat, S.; Mohammadi, M.B. Numerical study of the effect of turbulence on rate of reactions in the MILD combustion regime. *Combust. Theory Model.* **2011**, *15*, 753–772. https://doi.org/10.1080/13647830.2011.561368.
102. Hautman, D.J.; Dryer, F.L.; Schug, K.P.; Glassman, I. A Multiple-step Overall Kinetic Mechanism for the Oxidation of Hydrocarbons. *Combust. Sci. Technol.* **1981**, *25*, 219–235. https://doi.org/10.1080/00102208108547504.
103. Ranzi, E.; Frassoldati, A.; Stagni, A.; Pelucchi, M.; Cuoci, A.; Faravelli, T. Reduced Kinetic Schemes of Complex Reaction Systems: Fossil and Biomass-Derived Transportation Fuels. *Int. J. Chem. Kinet.* **2014**, *46*, 512–542. https://doi.org/10.1002/kin.20867.
104. San Diego Mechanism. Available online: https://web.eng.ucsd.edu/mae/groups/combustion/mechanism.html (accessed on 2 February 2022.
105. Sorrentino, G.; Sabia, P.; de Joannon, M.; Ragucci, R.; Cavaliere, A.; Göktolga, U.; van Oijen, J.; de Goey, P. Development of a Novel Cyclonic Flow Combustion Chamber for Achieving MILD/Flameless Combustion. *Energy Procedia* **2015**, *66*, 141–144. https://doi.org/10.1016/j.egypro.2015.02.079.
106. Ranzi, E.; Frassoldati, A.; Grana, R.; Cuoci, A.; Faravelli, T.; Kelley, A.P.; Law, C.K. Hierarchical and comparative kinetic modeling of laminar flame speeds of hydrocarbon and oxygenated fuels. *Prog. Energy Combust. Sci.* **2012**, *38*, 468–501. https://doi/org10.1016/j.pecs.2012.03.004.
107. Shabanian, S.R.; Medwell, P.R.; Rahimi, M.; Frassoldati, A.; Cuoci, A. Kinetic and fluid dynamic modeling of ethylene jet flames in diluted and heated oxidant stream combustion conditions. *Appl. Therm. Eng.* **2013**, *52*, 538–554.
108. Danon, B.; de Jong, W.; Roekaerts, D.J.E.M. Experimental and Numerical Investigation of a FLOX Combustor Firing Low Calorific Value Gases. *Combust. Sci. Technol.* **2010**, *182*, 1261–1278. https://doi.org/10.1080/00102201003639284.
109. Halouane, Y.; Dehbi, A. CFD simulations of premixed hydrogen combustion using the Eddy Dissipation and the Turbulent Flame Closure models. *Int. J. Hydrog. Energy* **2017**, *42*, 21990–2004
110. Agarwal, A.; Pitso, I. Modelling & numerical exploration of pulsejet engine using eddy dissipation combustion model. *Mater. Today Proc.* **2020**, *27*, 1341–1349.
111. Romero-Anton, N.; Huang, X.; Bao, H.; Martin-Eskudero, K.; Salazar-Herran, E.; Roekaerts, D. New extended eddy dissipation concept model for flameless combustion in furnaces. *Combust. Flame* **2020**, *220*, 49–62. https://doi.org/10.1016/j.combustflame.2020.06.025.
112. Dong, G.; Huang, Y.; Chen, Y. Study of effects of different chemical reaction mechanisms on computation results for methane jet turbulence diffusion flame. *J. Fuel Chem. Technol.* **2000**, *28*, 49–54.
113. Wei, J.; Ye, M.; Zhang, S.; Qin, J.; Haidn, O.J. Modeling of a 7-elements GOX/GCH4 combustion chamber using RANS with Eddy-Dissipation Concept model. *Aerosp. Sci. Technol.* **2020**, *99*, 10576. https://doi.org/10.1016/j.ast.2020.105762.
114. Jóźwiak, P.; Hercog, J.; Kiedrzyńska, A.; Badyda, K. CFD analysis of natural gas substitution with syngas in the industrial furnaces. *Energy* **2019**, *179*, 593–602.
115. Richter, A.; Vascellari, M.; Nikrityuk, P.A.; Hasse, C. Detailed analysis of reacting particles in an entrained-flow gasifier. *Fuel Process. Technol.* **2016**, *144*, 95–108. https://doi.org/10.1016/j.fuproc.2015.12.014.
116. Park, S.S.; Jeong, H.J.; Hwang, J. 3-D CFD Modeling for Parametric Study in a 300-MWe One-Stage Oxygen-Blown Entrained-Bed Coal Gasifier. *Energies* **2015**, *8*, 4216–4236, https://doi.org/10.3390/en8054216.
117. Zhang, N.; Chen, B.; Qiu, T. CFD simulation of cracking tube with internal twisted slices. In *11th International Symposium on Process Systems Engineering*; Karimi, I.A., Srinivasan, R., Eds.; Elsevier: Amsterdam, The Netherlands, 2012; pp. 905–909.
118. Sundaram, K.M.; Froment, G.F. Modeling of Thermal Cracking Kinetics. 3. Radical Mechanisms for the Pyrolysis of Simple Paraffins, Olefins, and Their Mixtures. *Ind. Eng. Chem. Fundam.* **1978**, *17*, 174–182. https://doi.org/10.1021/i160067a006.
119. Zhang, N.; Qiu, T.; Chen, B. CFD Simulation of Propane Cracking Tube Using Detailed Radical Kinetic Mechanism. *Chin. J. Chem. Eng.* **2013**, *21*, 1319–1331.
120. Ouyang, Y.; Xiang, Y.; Zou, H.; Chu, G.; Chen, J. Flow characteristics and micromixing modeling in a microporous tube-in-tube microchannel reactor by CFD. *Chem. Eng. J.* **2017**, *321*, 533–545. https://doi.org/10.1016/j.cej.2017.03.151.
121. Guihua, H.; Honggang, W.; Feng, Q. Numerical simulation on flow, combustion and heat transfer of ethylene cracking furnaces. *Chem. Eng. Sci.* **2011**, *66*, 1600–1611.
122. Tutar, M.; Üstün, C.E.; Campillo-Robles, J.M.; Fuente, R.; Cibrián, S.; Arzua, I.; Fernández, A.; López, G.A. Optimized CFD modelling and validation of radiation section of an industrial top-fired steam methane reforming furnace. *Comput. Chem. Eng.* **2021**, *155*, 107504. https://doi.org/10.1016/j.compchemeng.2021.107504.
123. Lbas, M.; Yılmaz, İ.; Kaplan, Y. Investigations of hydrogen and hydrogen–hydrocarbon composite fuel combustion and NOx emission characteristics in a model combustor. *Int. J. Hydrog. Energy* **2005**, *30*, 1139–1147.
124. Lan, X.; Gao, J.; Xu, C.; Zhang, H. Numerical Simulation of Transfer and Reaction Processes in Ethylene Furnaces. *Chem. Eng. Res. Des.* **2007**, *85*, 1565–1579.
125. Laubscher, R.; van der Merwe, S. Heat transfer modelling of semi-suspension biomass fired industrial watertube boiler at full- and part-load using CFD. *Therm. Sci. Eng. Prog.* **2021**, *25*, 100969
126. Gruber, T.; Scharler, R.; Obernberger, I. Application of an empirical model in CFD simulations to predict the local high temperature corrosion potential in biomass fired boilers. *Biomass Bioenergy* **2015**, *79*, 145–154. https://doi.org/10.1016/j.biombioe.2015.02.024.